Radar altimeter waveform simulations in Antarctica with the Snow Microwave Radiative Transfer Model (SMRT)

Fanny Larue, Ghislain Picard, Jérémie Aublanc, Laurent Arnaud, Alvaro Robledano-Perez, Emmanuel Le Meur, Vincent Favier, Bruno Jourdain, Joel Savarino, Pierre Thibaut

▶ To cite this version:

Fanny Larue, Ghislain Picard, Jérémie Aublanc, Laurent Arnaud, Alvaro Robledano-Perez, et al.. Radar altimeter waveform simulations in Antarctica with the Snow Microwave Radiative Transfer Model (SMRT). Remote Sensing of Environment, 2021, 263, pp.112534. 10.1016/j.rse.2021.112534 . hal-03402150

HAL Id: hal-03402150
https://hal.science/hal-03402150v1

Radar altimeter waveform simulations in Antarctica with the Snow Microwave Radiative Transfer Model (SMRT)

Fanny Larue[a], Ghislain Picard[a], Jérémie Aublanc[c], Laurent Arnaud[a], Alvaro Robledano-Perez[a,b], Emmanuel Le Meur[a], Vincent Favier[a], Bruno Jourdain[a], Joel Savarino[a], Pierre Thibaut[c]

[a] *Univ. Grenoble Alpes, CNRS, Institut des Géosciences de l'Environnement (IGE), UMR 5001, Grenoble, 38041, France*
[b] *Univ. Grenoble Alpes, Université de Toulouse, Météo-France, CNRS, CNRM, Centre d'Etudes de la Neige, 38000 Grenoble, France*
[c] *Collecte Localisation Satellites (CLS), 31520 Ramonville Saint-Agne, France*

Abstract

Radar altimeters are important tools to monitor the volume of the ice sheets. The penetration of radar waves in the snowpack is a major source of uncertainty to retrieve surface elevation. To correct this effect, a better understanding of the sensitivity of the radar waveforms to snow properties is needed. Here, we present an extension of the Snow Model Radiative Transfer (SMRT) to compute radar waveforms and conduct a series of simulations on the Antarctic ice sheet. SMRT is driven by snow and surface roughness properties measured over a large latitudinal range during two field campaigns on the Antarctic Plateau. These measurements show that the snowpack is rougher, denser, less stratified, warmer, and has smaller snow grains near the coast than on the central Plateau. These simulations are compared to satellite observations in the Ka, Ku, and S bands. SMRT reproduces the observed waveforms well. For all sites and all sensors, the main contribution comes from the surface echo. The echo from snow grains (volume scattering) represents up to 40% of the amplitude of the total waveform power in the Ka band, and less at the lower frequencies. The highest amplitude is observed on the central Plateau due to the combination

---

*Corresponding author
Email address: `ghislain.picard@univ-grenoble-alpes.fr` (Ghislain Picard)

Preprint submitted to Elsevier *April 11, 2021*

of higher reflection from the surface, higher scattering by snow grains in the Ka and Ku bands, and higher inter-layer reflections in the S band. In the Ka band, the wave penetrates in the snowpack less deeply on the central Plateau than near the coast because of the strong scattering caused by the larger snow grains. The opposite is observed in the S band, the wave penetrates deeper on the central Plateau because of the lower absorption due to the lower snow temperatures. The elevation bias caused by wave penetration into the snowpack show a constant bias of 10 cm for all sites in the Ka band, and a bias of 11 cm, and 21 cm in the Ku band for sites close to the coast and the central Plateau, respectively. Now that SMRT is performing waveform simulations, further work will address how the snowpack properties affect the parameters retrieved by more advanced retracking algorithms such as ICE-2 for different snow cover surfaces.

Keywords: Antarctic ice sheet, SMRT, remote sensing, radar altimetry, waveform, modeling, field measurements

1. Introduction

Radar altimeters are active sensors emitting microwave pulses and measuring the backscattered energy as a function of time, providing the so-called waveform. The surface elevation is deduced from this two-way travel time, once the surface echo has been precisely identified in the waveform (Rémy and Parouty, 2009). Initially developed for sea level monitoring, altimeter observations were rapidly employed for measuring the surface elevation of the ice sheets to monitor surface mass balance changes and hence the contribution to the global sea level (Bindschadler and Zwally, 1986, Zwally, 1989, Helm et al., 2014). However, additional processes specific to the ice sheets such as the penetration of the wave into the snowpack for instance, limit the accuracy of the inferred elevation (Partington et al., 1989, Legrésy and Rémy, 1997, Rémy and Parouty, 2009). A better understanding of how the wave interacts with the snowpack and how the waveform is affected by the snowpack properties is required to improve retracking algorithms in the future.

On the ice sheets, the radar waveform is the addition of the echo coming from the upper air-snow interface (”surface echo”), and diffuse echoes from the snowpack due to reflections at the internal layer interfaces (”internal interface echoes”) and due to scattering by snow grains (”volume echo”) (Brown, 1977, Partington et al., 1989). The surface echo is mainly controlled by the topography that influences the illuminated radar footprint (Brenner et al., 1983), and by the surface roughness features having a size close to or larger than the radar wavelength (i.e. above 10 cm in the S band, hereinafter referred to as centimeter-scale roughness) (Remy and Minster, 1991). Rougher surfaces induce a weaker backscatter than smooth ones (Van Der Veen et al., 1998, Van Der Veen et al., 2009, Rosmorduc et al., 2011, Kurtz et al., 2014, Smith and Vericat, 2015, Smith et al., 2016). The volume echo depends on the wave penetration and the mechanisms of scattering and absorption in the snowpack (Remy et al., 2012). The radar wave penetrates a few meters within the snowpack at high frequencies (>13 GHz) and even deeper at lower frequencies (Legrésy and Rémy, 1997). The wave is scattered by snow grains according to their sizes and to the wave frequency and by internal layering according to the density contrasts between the successive layers, while the absorption losses depend on snow temperature and the wave frequency mainly (Adodo et al., 2018). The snow properties greatly vary in space and time across the Antarctic continent, making it difficult to accurately quantify the variations of volume echo (Partington et al., 1989, Legrésy and Rémy, 1997, Guerreiro et al., 2017). Recently, Guerreiro et al. (2016) and Guerreiro et al. (2017) showed that combining altimeter observations at several frequencies (Ka and Ku bands) helps to characterize the volume echo. The idea is to exploit the fact that the penetration depth of the wave is larger at lower frequencies, which in turn makes it possible to untangle the respective contributions from the surface and from inside the snowpack and consequently correct the inferred surface elevation error due to the volume echo.

Several waveform models have been developed to investigate the radar signal over the ice sheets (Newkirk and Brown, 1992, Femenias et al., 1993, Adams and Brown, 1998). As for the ocean, the backscattered energy from the surface is estimated with the Brown surface scattering model (Brown, 1977). This model works for altimeters operating in Low-Resolution Mode (LRM). For a perfectly flat and smooth area, the Brown model takes into account the fact that the spherical wave emitted by the radar first hits the surface at nadir, and then successively hits concentric areas of increasingly larger radius. The echo is calculated by summing over the delayed reflections from all elementary concentric areas. Several methods have been developed to consider the surface roughness in the echo calculation according to the incident wavelength, such as the Geometrical Optics (GO) approximation (Tsang et al., 2001) for large scale roughness and the Integral Equation Method (IEM) theory (Fung et al., 1992) for small scale roughness. To simulate the backscattered energy from the snowpack, the models of Partington et al. (1989), Newkirk and Brown (1992), Davis and Moore (1993), Femenias et al. (1993), and Legrésy and Rémy (1997) compute the loss factor that represents the wave attenuation in the snowpack. However, these models assume a homogeneous snowpack. To account for the heterogeneity Adams and Brown (1998) developed a new model based on the Brown surface model (AB98 model hereinafter) that extends horizontally the volume echo with the average scattering properties of each snow layer. Lacroix et al. (2007) and Lacroix et al. (2008a) proposed a waveform model (L08 hereinafter) adapted from AB98, that calculates volume scattering with an electromagnetic model to relate the density and correlation length to the scattering properties following Mätzler and Wegmuller (1987). However, the L08 model represents the snow microstructure as a collection of independent ice spheres, which is known to be unrealistic (Wiesmann and Mätzler, 1999). Unfortunately, all these existing models have not been extensively validated because they were applied in a limited number of studies and not made widely available to the community. Consequently, their usability is relatively low.

Here we propose to extend the Snow Model Radiative Transfer model (SMRT) to conduct waveform simulations on the Antarctic ice sheet. The aim of the paper is twofold 1) evaluate the model performances in the Ka, Ku, and S bands in Antarctica and 2) investigate how the penetration depth of the wave depends on snow properties and estimate the induced elevation bias. SMRT is a passive and active microwave model for multi-layered snowpack and other cold environments such as sea-ice (Picard et al., 2018). The active mode only computes a time-independent total backscattering coefficient and is therefore not suitable for altimetry. A module dedicated to altimetry is presented here to compute the wave propagation within the snowpack as a function of time by solving the time-dependent radiative transfer equation. The module is also combined with the Brown model to account for the wave sphericity and yields the waveform as measured by altimeters. Besides, the echoes from the surface, internal interfaces, and snow grain are separately provided. The proposed module was easily integrated into SMRT without redeveloping a complete model because the implementation is structured and modular offering the possibility to switch between (i) different electromagnetic models, (ii) different snow microstructure representations to simulate volume scattering, and (iii) different methods to solve the radiative transfer equation (the so-called RT solver). The existing code of the model and its extension are open sources (`http://www.smrt-model.science/`, last access: 23/02/2021).

SMRT requires as input the snow density, temperature, grain size, and thickness of each layer up to several meter depth. In this study, these properties were measured on ≈ 8 m ice cores extracted at seven sites spanning a large latitudinal range on the Antarctic Plateau, from 68,7° S to 79,9° S, during two extensive field campaigns on the Antarctic Plateau. The simulation of surface scattering requires also a precise quantification of surface roughness at centimeter scales (Lacroix et al., 2008a,b, Studinger et al., 2020). Such measurements are scarce in Antarctica. Laser scanning devices commonly used to take such measurements in temperate climates are difficult to operate in the cold (Kerr et al., 2009, Nield et al., 2013). Recently, Irvine-Fynn et al. (2014) and Smith et al. (2016) proposed a simple protocol using a commercial camera and photogrammetry to retrieve high-resolution point clouds over small areas on glacier surfaces. We adapted this protocol to retrieve surface roughness parameters with a horizontal spacing distance of 9 cm. The simulated waveforms are evaluated with the satellite observations recorded in the conventional altimeter pulse-limited mode (LRM mode), by the SARAL-AltiKa altimeter in the Ka band, the ENVISAT dual-frequency radar altimeter in the Ku and S bands, and the Sentinel-3A Synthetic Aperture Radar Altimeter (SRAL) instrument in the Ku band (initially acquired in delay-doppler mode and then emulated in pseudo-LRM mode).

The altimeter extension is detailed in Section 2. The study sites, in-situ measurements, satellite observations and simulation framework are presented in Section 3. In Section 4, the performance of the model is analyzed, and the sensitivity of the waveform and the wave penetration depth to the snowpack properties, as well as the induced elevation bias, are investigated using SMRT. Moreover, a simple optimisation is proposed by adjusting the roughness parameter. The discussion in Section 5 addresses the relationship between the radar waveform shape and meteorological conditions impacting the snowpack properties, as well as the limitations of the simulations. One possible approach to simulate altimeter waveforms when no in-situ measurements are available is also discussed.

SMRT opens the way to better interpret the radar waveforms on the polar ice sheet - and even on other snow covers - and thus refine the estimation of its mass balance.

2. Theory

The radar theory is presented in Section 2.1. The method developed to compute the waveform is explained in Sections 2.2 and 2.3 and its implementation in SMRT is detailed in Section 2.4.

2.1. The radar waveform of the Antarctic ice sheet

In LRM, the radar altimeter sends pulses and records the echoes from both the surface and subsurface, which is used to estimate the returned power $P_r(t)$ as a function of time t, the so-called waveform. Over a snow rough surface, the wave penetrates in the snowpack and the average return power follows Adams and Brown (1998) and Legresy et al. (2005):

$$P_r(t) = pdf(t) \otimes [P_{\mathrm{FS}}(t) + P_{\mathrm{int}}(t) + P_{\mathrm{vol}}(t)] \otimes P_t(t) \tag{1}$$

where *pdf* is the specular point height probability density function that accounts for the surface height variability, $\otimes$ is the convolution operator, and P_t represents the transmitted signal power. P_{FS} is the flat impulse response of the surface echo (as in Adams and Brown (1998) and Lacroix et al. (2008a)), P_{int} and P_{vol} are the flat impulse response of the echoes from the internal interfaces and from the scattering by snow grains (volume scattering), respectively. The internal interfaces are the separation between the homogeneous layers of the snowpack as illustrated in Figure 1a.

The Eq. 1 is equivalent to:

$$P_r(t) = pdf(t) \otimes P_{\mathrm{FIR}}(t) \otimes \left[\sigma_s^0 \delta(t) + I_{\mathrm{int}}(t) + I_{\mathrm{vol}}(t)\right] \otimes P_t(t) \tag{2}$$

where σ_s^0 is the backscattering coefficient of the surface. I_{int} and I_{vol} are the specific intensities (or radiance) coming from the interface reflections and volume scattering, respectively. $P_{\mathrm{FIR}}(t)$ is the flat impulse response that propagates horizontally the scattering sources, computed with the classical radar equation integrated over the illuminated surface according to the Brown model:

$$P_{\mathrm{FIR}}(t) = \frac{\lambda^2}{(4\pi)^3} \int_A \left(\frac{G^2(\theta)}{r^4} \right) dA \tag{3}$$

where λ is the radar wavelength, and $dA = \rho \, d\rho \, d\psi$ the elementary area at time t, with ψ the incident zenith angle of the pulse and ρ the horizontal distance between the z axis and dA. θ is the angle from the antenna boresight axis (the off-nadir) to the line from the sensor to dA. It is a function of time. r is the distance between the sensor and dA. The geometry of the problem is described in figure 1 of Brown (1977). If the off-nadir is negligible, we have $\psi \approx \theta$. G(θ) is the antenna pattern modeled with a azimuthally symmetric Gaussian beam as $G(\theta) = G_0 \; e^{-(2/\gamma)\sin^2\theta}$ with G_0 the peak antenna gain at boresight ($G_0 = 1$ here) and $\gamma = 2\sin^2(\theta_{3dB}/2) \; / \ln 2$ determined from the 3

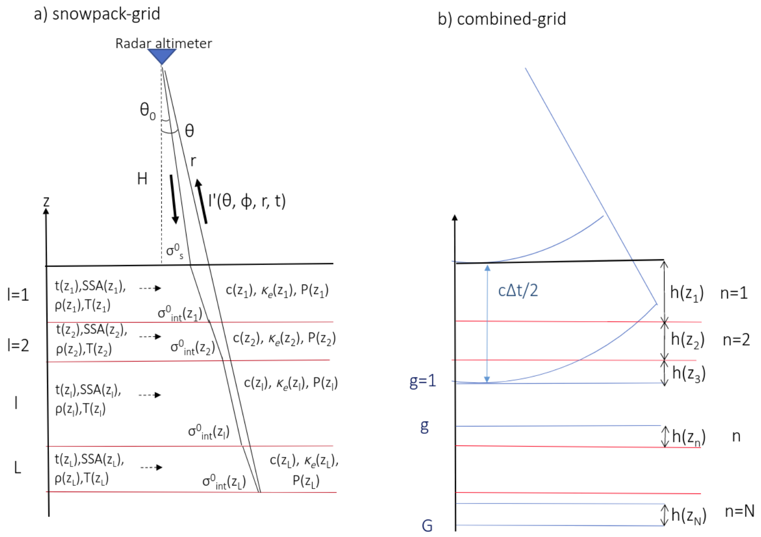

Figure 1: Medium geometry and the grids used for the modeling: a) The snowpack-grid (red lines) is defined by the homogeneous layers of the snowpack, described with SSA(z), density ρ(z), temperature $T(z)$ and thickness $t(z)$ at depth z, with l the snow layer index at depth z and L the total number of layers crossed by the radar wave. b) two grids are represented: At left the altimeter-grid (blue lines) is defined by the altimeter gates that are described with a thickness of $c(z)\Delta t/2$, g is the gate index at depth z, and G is the total number of altimeter gates crossing the snowpack; and at right the combined-grid results from merging the snowpack-grid and the altimeter-grid (combining both blue and red lines), where n is the index of the combined-grid and N is the total number of sublayers above z_N.

dB beamwidth (Brown, 1977). In the presence of a local slope θ_s, the incident angle θ is changed to $\theta_s + \theta$ in P_{FIR}.

The equation for P_{FS} is given in Newkirk and Brown (1992). The effect of the Earth's finite curvature is taken into account by including the factor $1/(1 + H/R)$, with R the earth's radius as detailed in appendix A of Newkirk and Brown (1992).

In Eq. 2, the *pdf* is estimated assuming that the specular point height follows a Gaussian and is written as follows (Brown, 1977):

$$pdf(t) = \exp\left(\frac{-t^2}{2(2\sigma_{\text{surf}}/c_0)^2}\right) \tag{4}$$

with c_0 is the speed of light in air, and σ_{surf} the root mean square heights (rms) of the surface topography (relative to the mean level). σ_{surf} represents ground elevation variations over the footprint at a large scale.

P_t is approximated with a Gaussian function:

$$P_t(t) = \exp\left(\frac{-t^2}{2\sigma_p^2}\right) \tag{5}$$

where $\sigma_p = 0.513\Delta t$ as defined by MacArthur (1978). Δt is the altimeter gate sampling rate, the inverse of the pulse bandwidth of the sensor. This Gaussian approximation is adequate due to the shortness of the emitted pulse Brown (1977) but it neglects the sidelobes of the antenna.

The convolution with $P_t(t)$ and $pdf(t)$ is computed using the approximation proposed by Brown (1977) which assumes small gate sampling rate ($< 20\,\mathrm{ns}$ - which is the case for typical short pulse radar altimeters - (Brown, 1977)) and surface rms height.

2.2. Calculation of vertical distributions of specific intensities

The general form of the radiative equation in the snowpack writes (Adams and Brown, 1998):

$$\begin{aligned}\frac{1}{c(\mathbf{r})}\frac{\partial}{\partial t}I'(\theta,\phi,\mathbf{r},t) + \frac{\partial}{\partial s}I'(\theta,\phi,\mathbf{r},t) &= -\kappa_{\mathrm{e}}(\mathbf{r})I'(\theta,\phi,\mathbf{r},t)\\ &+\frac{1}{4\pi}\int_{4\pi}P(\theta,\theta',\phi-\phi',\mathbf{r})I'(\theta',\phi',\mathbf{r},t)d\Omega'\end{aligned} \tag{6}$$

with $d\Omega' = \sin\theta' d\theta d\phi$, where θ and ϕ are the propagation zenith and azimuth angles and Ω the solid angle. s is the curvilinear abscissa along the trajectory. $I(\mathbf{r}) = I'(\mathbf{r})/n^2$ is the reduced specific intensity at position $\mathbf{r}$ within the medium with refractive index $n(\mathbf{r})$. $I'(\mathbf{r})$ is the specific intensity of the wave or radiance (the unknown quantity of the equation). Both are expressed in $\mathrm{W\,m^{-2}\,Hz^{-1}\,sr^{-1}}$ units. The normalization by n^2 accounts for the divergence of the beam due to refraction so that I' is constant between each side of any interface separating two layers with different refraction indexes $n(\mathbf{r})$. Conversely, the conventional radiance I is not constant (Fig. 1). Here, the polarization is neglected because of the near-nadir incidence (Adams and Brown, 1998). The medium is assumed isotropic so that the extinction coefficient κ_e is independent of θ and the phase matrix P only depends on the difference between the azimuths $(\phi - \phi')$, instead of the two azimuths separately. c is the speed of the wave in the medium at the distance r, which is related to the vertical permittivity profile of the snow.

The medium is depicted in Figure 1. The continuity conditions at the layer interface located at a distance r_l writes:

$$I'(\theta, \phi, \mathbf{r}_l^+, t) = T(\mathbf{r}_l, \theta) I'(\theta, \phi, \mathbf{r}_l^-, t) \tag{7}$$

where $\mathbf{r}_l^+$ and $\mathbf{r}_l^-$ are the positions just above and below the layer interface l. $T(\mathbf{r}_l, \theta) = 1 - R(\mathbf{r}_l, \theta)$ is the transmittance (for the reduced specific intensity) at the position $\mathbf{r}_l$ and R is the reflection coefficient. The echo is a combination of specular reflection and diffuse surface scattering.

Assuming the propagation in the medium is nearly vertical ($\theta \approx 0$) leads to $s = r = z$ and $\cos\theta = 1$ with a $\mathcal{O}(\theta^2)$ accuracy. For a typical space-borne altimeter at $\sim 800\,\mathrm{km}$ altitude, with a beam half width of $1.3°$, this approximation is equivalent to a maximal error of $3\,\mathrm{mm}$ at $10\,\mathrm{m}$ depth, which is negligible, for instance compared to the localization error of the in-situ measurements.

The 0^{th}-order radiative transfer equation is obtained by neglecting the source term in Eq. 6 ($P^{0^{th}} = 0$) and writes :

$$\frac{1}{c(z)} \frac{\partial}{\partial t} I^{0^{\mathrm{th}}}(\theta, z, t) + \frac{\partial}{\partial z} I^{0^{\mathrm{th}}}(\theta, z, t) = -\kappa_{\mathrm{e}}(z) I^{0^{\mathrm{th}}}(\theta, z, t). \tag{8}$$

Solving for the z variable and then integrating over t gives the 0^{th}-order intensity at depth z (i.e the downwelling intensity at depth z):

$$I^{0^{\mathrm{th}}}(\theta, z, t) = E_0 \left(t - \int_0^z \frac{dz}{c(z)} \right) \delta(\cos\theta_0) \exp\left(- \int_0^z \kappa_{\mathrm{e}}(z) dz \right) \prod_{l=1}^{L(z)} T(z_l) \tag{9}$$

where $E_0(\theta_0, z, t)$ is the incident flux (in $\mathrm{W\,m^{-2}\,Hz^{-1}}$) transmitted by the altimeter just above the surface at time t, propagating in the near-nadir direction θ_0. The flux E_0 in Eq. 9 is considered with a time delay that depends on the path and the speed of the wave in the medium. $I^{0^{\mathrm{th}}}$ has the form of a downwelling wave, with an exponentially decreasing intensity. The exponential term represents the attenuation of the signal due to the extinction of the wave in the snowpack from the surface to the depth z. The product series represents the attenuation due to the interface transmittance T. z_l is the depth of the snow layer l (Fig. 1a). $L(z)$ is the number of snow layers between the surface and the depth z (Fig. 1a). δ represents the Dirac distribution.

The 1st-order solution only includes the direct backscattered wave emerging at the surface from volume scattering. It is written $I_{\mathrm{vol}}^{1^{\mathrm{st}}}(z=0,t)$ and obtained by inserting the 0th-order solution into the source term in Eq. 6, solving the differential equation in z and t, and finally integrating over z from the surface to the bottom of the medium $(z = H)$. This yields:

$$\begin{aligned} I_{\mathrm{vol}}^{1^{\mathrm{st}}}(z=0,t) = \int_0^H \Bigg(& E_0\left(t - 2\int_{z=0}^{z} \frac{dz'}{c(z')}\right) \frac{1}{n^2(z)} \frac{P(0,0,\pi,z)}{4\pi} \\ & \exp\left(-2\int_{z=0}^{z} \kappa_{\mathrm{e}}(z')dz'\right) \prod_{l=1}^{L(z)} T(z_l)^2 \Bigg) dz \end{aligned} \tag{10}$$

where $P(0,0,\pi,z)$ is the scattering function from snow grains in the backward direction at nadir incidence. The dependence on θ is neglected because snow grains are much smaller than the wavelength, resulting in a smooth Rayleigh-type phase diagram (Tsang et al., 1985). The term $\frac{1}{n^2(z)}$ comes from the integration of $\delta(\cos\theta_0)$ over θ at depth z in Eq. 6, using the change of variable θ to θ_0 and Snell law ($\cos\theta_0 = \sqrt{1 - n^2(z)(1-\cos^2\theta)}$). In Eq. 10, the 1st-order backscatter from the volume (i.e. coming from the snow grains within the upper ice firn and bubbles in the ice below) is the vertical integral of the local backscatter (the term with the phase matrix P), attenuated from the surface to depth z with the extinction κ_e (the exponential term) and attenuated by the two-way transmission $T(z_l)^2$ at each interface. The two-way delay is included in the E_0 term.

To solve the integral over z, the medium is discretized on a new grid, called "combined-grid", which merges the physical snow layers l and the altimeter gates g as depicted in Fig. 1b. Each new sublayer n of the combined-grid at depth z_n is 1) fully included in one of the homogeneous layers l of the snowpack (implying that c, κ_e and P are constant) and 2) is thin enough to neglect the propagation time (i.e. with a thickness $h(z_n) = \frac{c_0}{n(z_n)} \frac{\Delta t}{2} \ll c/B$). It follows that E_0 variations within each sublayer are negligible, and the term can be taken out of the integral. The volume backscattered intensity $I^{1^{\text{st}}}_{\text{n, vol}}(z = 0, t)$ emerging at the surface and coming from the sublayer n is then given by the difference of Eq. 10 between the top and bottom of the sublayer:

$$\begin{aligned} I^{1^{\text{st}}}_{\text{n, vol}}(z = 0, t) = E_0 \left(t - 2 \int_0^{z_n} \frac{dz'}{c(z')} \right) \frac{1}{n(z_n)} \frac{P(0, 0, \pi, z_n)}{4\pi} \\ \frac{1 - \exp\left(-2\kappa_{\text{e}}(z_n) h(z_n)\right)}{\kappa_{\text{e}}(z_n)} \exp\left(-2 \int_0^{z_n} \kappa_{\text{e}}(z') dz' \right) \prod_{i=1}^{N} T(z_i)^2 \end{aligned} \tag{11}$$

N is the number of sublayers between the surface and the depth z_n reached at time t. The inner integrals over z' are then calculated. The integrals are converted into discrete sums:

$$\begin{aligned} I^{1^{\text{st}}}_{\text{n, vol}}(z = 0, t) = E_0 \left(t - 2 \sum_{n'=1}^{n-1} \frac{h(z_{n'})}{c(z_{n'})} \right) \frac{1}{n(z_n)} \frac{P(0, 0, \pi, z_n)}{4\pi} \\ \frac{1 - \exp\left(-2\kappa_{\text{e}}(z_n) h(z_n)\right)}{\kappa_{\text{e}}(z_n)} \exp\left(-2 \sum_{n'=1}^{n-1} \kappa_{\text{e}}(z_{n'}) h(z_{n'}) \right) \prod_{i=1}^{N} T(z_i)^2. \end{aligned} \tag{12}$$

Following a similar approach, the backscattered intensity from the internal interfaces $I^{1^{\text{st}}}_{\text{n, int}}(z = 0, \theta, t)$ emerging at the surface and coming from the sublayer n is given by:

$$\begin{aligned} I^{1^{\text{st}}}_{\text{n, int}}(z = 0, \theta, t) = E_0 \left(t - 2 \sum_{n'=1}^{n-1} \frac{h(z_{n'})}{c(z_{n'})} \right) \frac{1}{n(z_{n-1})} \frac{\sigma^0_{\text{int}}(\theta, z_n)}{4\pi} \\ \frac{1 - \exp\left(-2\kappa_{\text{e}}(z_n) h(z_n)\right)}{\kappa_{\text{e}}(z_n)} \exp\left(-2 \sum_{n'=1}^{n-1} \kappa_{\text{e}}(z_{n'}) h(z_{n'}) \right) \prod_{i=1}^{N} T(z_i)^2. \end{aligned} \tag{13}$$

where $\sigma^0_{\text{int}}(\theta, z_n)$ is the backscattering coefficient of the interface at depth z_n. This coefficient must be estimated with an appropriate surface scattering model considering the scale of the surface and interface roughness, and the incident wavelength. As detailed further, two methods are available in the current SMRT version: the IEM theory adapted to roughness scales of the same order as the wavelength, and the Geometrical Optics (GO) approximation for larger-than-wavelength roughness. The dependence on the incidence angle θ is not neglected here because interface scattering near nadir variations are usually sharp ($\mathcal{O}(\theta)$) as opposed to that of volume scattering ($\mathcal{O}(\theta^2)$ or less).

2.3. Propagation between the altimeter and the surface

To account for the delay introduced by the spherical wave spread over the surface, the intensities backscattered from the internal interfaces and the snow grains, emerging at the surface, are further convoluted with the flat impulse response P_{FIR} (Eq. 2). This yields:

$$P_{\mathrm{X}}(t) = \frac{\lambda^2}{(4\pi)^3} \int_A \frac{\delta(t - t_s) G^2(\theta_0)}{r^4} dA \sum_{n=1}^{N} I^{1^{\mathrm{st}}}_{\mathrm{n,\ X}}(z = 0, \theta, t - t_s). \tag{14}$$

where $t_s = 2r/c_0$ is the two-way time between the altimeter and the wave hit position on the surface. The index X denotes here either int or vol depending on the application. This equation is solved by expanding $dA = \rho d\rho d\psi$, integrating over ψ, and making the change of variable ρ to r using $r^2 = H^2 + \rho^2$, with H the satellite altimeter height. We assumed $\frac{r}{r^4} \approx \frac{1}{H^3}$ which corresponds to a maximal error of 3 mm at 10 m. Finally we made the change of variable r to t using $r = \frac{ct'}{2}$, considering t' as the two-way time between the altimeter and the wave hit position in the snowpack. It yields:

$$P_{\mathrm{X}}(t) = \frac{\lambda^2 c_0}{4(4\pi)^2 H^3} \int_0^{\infty} dt' G^2(\theta_0(t')) \sum_{n=1}^{N} I^{1^{\mathrm{st}}}_{\mathrm{n,\ X}}(z = 0, \theta_0(t'), t - t') \tag{15}$$

where $\theta_0(t') = \tan^{-1} \sqrt{\frac{ct'}{H} - 2}$.

To compute the signal received by the altimeter for each gate, the combined-grid is used. Recalling that the time in each sublayer of the combined grid is very small and can be assumed constant, the integral is transformed into a discrete sum:

$$P_{\mathrm{X}}(g\Delta t) = \frac{\lambda^2 c_0 \Delta t}{4(4\pi)^2 H^3} G^2(\theta_0(g\Delta t)) \sum_{n=1}^{N} I^{1^{\mathrm{st}}}_{\mathrm{n,\ X}}(z = 0, \theta_0(g\Delta t), t - g\Delta t) \tag{16}$$

with g the altimeter gate number index (e.g. 0 … 128 for the ENVISAT altimeter in the Ku band and the SARAL-AltiKa altimeter in the Ka band, and

0 . . . 64 for the ENVISAT altimeter in the S band) between the surface and the depth z (Fig. 1), and Δt the wave travel time between each gate.

At last, Eq. 5, 4, and 16 are combined to compute the average total returned power $P_r(t)$. The equation is valid for nadir-looking LRM sensors and accounts only for the first order backscatter. Modeling altimeters using SAR technique and accounting for higher order backscatter are let to further work.

2.4. Implementation in the Snow Microwave Radiative Transfer model

2.4.1. SMRT existing components

The SMRT model is a passive and active microwave model for multi-layered snowpacks in the range 1–200 GHz (Picard et al., 2018). It takes as input i) the characteristics of the sensor (active or passive, frequency, polarization, incidence angle), ii) the snow properties of each layer (thickness, density, temperature, and microstructure parameters as well as the liquid water content), iii) the properties of the underlying surface (roughness, the type of material, wetness, salinity, etc.).

The model works by first estimating the electromagnetic parameters governing the propagation in each layer and at each interface. This comprises for each layer z_l the computation of the extinction coefficients $\kappa_e(z_l)$, the phase matrix $P(0, 0, \pi, z_l)$, the propagation constant $c(z_l)$ according to the snow microstructure description and the electromagnetic model chosen by the user. Several electromagnetic models are implemented in SMRT, and the Improved Born approximation (IBA) (Mätzler, 1998) was used in the present study. For the interfaces, this comprises the computation of reflection and transmission coefficients ($R_(z_l)$ and $T(z_l)$) according to the type of model (e.g. Fresnel coefficients for flat surfaces, ...) and the interface roughness as well as the permittivity on each side of the interface. To compute the rough surface and interface backscattering coefficient σ_0, two surface scattering models were recently implemented in SMRT: the IEM theory (Fung et al., 1992) applicable when the roughness scales are of the same order as the wavelength, and the GO approximation (Tsang et al., 2001) for larger roughness. The input parameters needed to describe the roughness features depend on the selected method: the IEM theory requires the standard deviation of the height distribution (σ_h) and the horizontal correlation length (l), while the GO approximation requires the Mean Square Slopes of the surface (MSS). To run SMRT, each interface can be prescribed independently with different roughness values and even a surface scattering model if the roughness scale were very different. However, for sake of simplicity, we selected the GO approximation here which is the most adequate for the roughness data we have collected in the field (see Section 3.5.1).

The next and last step is the application of the Discrete Ordinate Method (DORT) to solve the radiative transfer equation, by taking into account either the thermal emission for the passive mode or an incident wave for the active mode. This last step is the one where SMRT was extended to account for the time travel of the spherical penetrating wave using Eq. 16 and thus predicting the radar waveform.

2.4.2. Implementation of the LRM altimetry solver in SMRT

The new "nadir LRM altimetry" module computes the outgoing specific intensity as a function of the wave travel time. In the first step, the extinction in each sublayer and the transmission through the interfaces are estimated with an electromagnetic model and combined to compute the downwelling intensity from the surface to each layer (Eq. 9). The backscatter due to volume scattering from every sublayer is then propagated upward considering the attenuation with Eq. 12. Similarly, the σ^0 are estimated for each interface (surface and internal interfaces) by accounting for the roughness, and the echoes due to interface and surface scattering are computed with Eq. 13. The output of this first step is the volume, surface, and interface specific intensities emerging at the surface as a function of time (or altimeter gates).

The model then accounts for the sphericity of the wave (Brown model) through the convolution with P_{FIR} (Eq. 3, where the earth curvature effect is taken into account), the surface topography with the *pdf* (Eq. 4, with the σ_{surf}) and the pulse shape with the P_t (Eq. 5). The sensor parameters (namely antenna pulse, beamwidth, bandwidth, mean altitude, etc.) are taken into account at this stage. $P_r(t)$ is deduced by numerical convolution (Eq. 2).

As output, SMRT generates the total returned power $P_r(t)$, and optionally the respective contributions of the volume, the surface, and the internal interfaces. It is also possible to disable the convolution computation to output the vertical backscattering profiles $I^{1^{\mathrm{st}}}_{\mathrm{n,\,X}}$ only as if the altimeter had a perfectly narrow beam (infinite gain antenna). This latter option is useful to investigate how the penetration depth of the wave is impacted by interface and volume scattering. The SMRT model and its new altimetry extension are open sources (www.smrt-model.science/, last access: 23/02/2021).

3. Materials and methods

Several datasets of in-situ measurements and satellite observations have been collected to run and evaluate the new altimetry extension of SMRT. The study area is detailed in Section 3.1. The measurements of snow properties and surface roughness are described in Sections 3.2 and 3.3. The satellite observations are introduced in Section 3.4. Finally, the simulation framework is explained in Section 3.5.

3.1. The study area

In-situ measurements were acquired during two field campaigns in Antarctica located in Figure 2 and Table 1. The selected sites include five stops of the French ASUMA traverse (Accuracy of the Surface Mass balance of Antarctica) carried out in December 2016 in Adelie Land (from 67° S to 70° S, Fig. 2), and two stops of the international EAIIST traverse (East Antarctic International Ice Sheet Traverse) carried out in December 2019 in the megadune area between the French–Italian research station Concordia and South Pole, over the central Plateau, one of the dryest part of Antarctica (from 77° S to 80° S, Fig. 2).

The local surface slope and the σ_{surf} of Eq. 4 were estimated from the Reference Elevation Model of Antarctica (REMA), over a 2 km radius circular area around each site. REMA is a high-resolution Digital Surface Model (DSM) of Antarctica at a 8 m spatial resolution with a typical elevation error of less than 1 m for tiles of 100 km × 100 km (Howat et al., 2019). Finer undulations of the surface (stastrugi,. . .) are not captured in our σ_{surf} estimates. Values are detailed in Table 1 for each site.

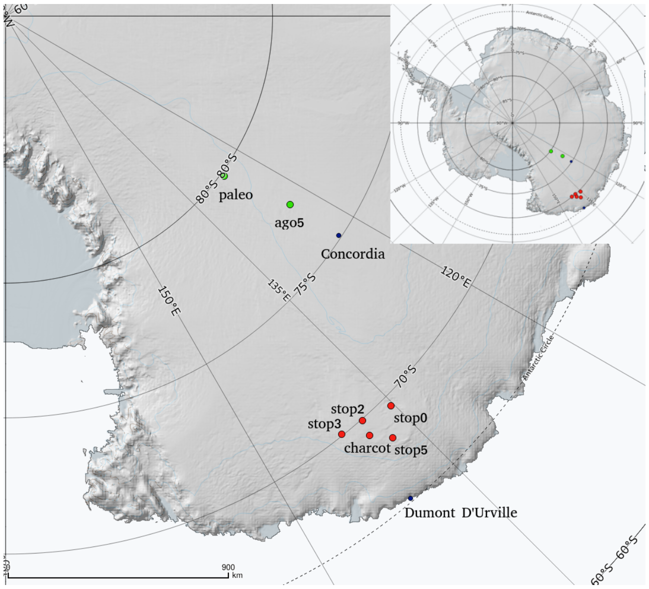

Figure 2: Location of the sites investigated during the ASUMA traverse in 2016 (red) and the EAIIST traverse in 2019 (green). The blue dots are the French–Italian research station Concordia and the French research station Dumont D'Urville.

Table 1: Characteristics of the studied sites: names, geographic coordinates (latitude and longitude), slopes (in degrees), rms height of the surface topography (σ_{surf}, in meters), the measured annual temperature T (in degrees Celsius), the MSS (Mean Square Slope), the mean Specific Surface Area of snow grains (SSA, in $\mathrm{m^{-2}\,kg^{-1}}$) and the mean density (ρ, in $\mathrm{kg\,m^{-3}}$) for the first 8 meters of snow. The '$^{\mathrm{A}}$' or '$^{\mathrm{E}}$' exponents indicate whether the site belongs to the ASUMA traverse or the EAIIST traverse, respectively.

Name	Latitude	Longitude	Slope	σ_{surf}	T	MSS	SSA	ρ
stop5^{A}	-68.75	137.44	0.02	0.31	-37.2	0.03	11.6	448
charcot^{A}	-69.38	139.02	0.13	0.33	-37.9	0.02	12.0	433
stop0^{A}	-69.64	135.28	0.01	0.18	-41.1	0.02	12.4	437
stop2^{A}	-69.95	138.55	0.05	0.34	-40.4	0.03	12.4	449
stop3^{A}	-70.06	141.20	0.21	0.45	-38.9	0.05	11.5	446
ago5^{E}	-77.24	123.48	0.09	0.32	-54.4	0.01	7.4	361
paleo^{E}	-79.85	126.20	0.08	0.30	-50.5	0.01	7.7	392

3.2. Measurements of the snow properties

SMRT was driven by the measured vertical profiles of density, layer thickness, temperature, and Specific Surface Area (SSA). The latter parameter was then related to the optical radius of snow grains r_{opt} (Gallet et al., 2011). At every site, 2 m core samples were extracted until 8 m depth with a 10 cm diameter drill. The cores were processed immediately during the traverses in a mobile cold laboratory. The measurements of the vertical profiles of SSA were acquired with the Alpine Snowpack Specific Surface Area Profiler (ASSSAP) instrument. The 1 m long cores were positioned on a horizontal bench and the ASSSAP instrument was slowly translated by hand 2 cm above the core, on a fixed horizontal rail. The SSA was recorded every 10 ms which corresponds to a resolution of about 1 mm. In practice, the effective resolution is coarser, due to the footprint of the laser used for the measurement (1 cm in diameter). This protocol was adapted from Arnaud et al. (2011) and Libois et al. (2015). ASSSAP records infrared reflectances at 1310 nm, which are converted in SSA values with an accuracy of 10 % (Arnaud et al., 2011).

For the snow density measurements, the cores were sliced every 10 cm. The diameter and height of each cylinder were measured with a caliper (precision of 0.1 mm), and the mass was measured with a scale (precision of 0.1 g). The overall uncertainty on the density measurements is 4%. The top and bottom 5 centimeters of each 2 m core were sometimes corrupted because of the core catchers. The density of these parts was not measured. They were discarded after measuring their exact lengths to allow precise positioning of the piece. The density profiles were then interpolated to fill the data gaps. Also, due to the thickness of the saw blade used to cut the ice core every 10 cm, we lost on average 4 mm of the core at each cylinder cut, i.e. 4 cm per meter. This has no impact on the overall profile since it is taken into account in the calculation of the density profile.

The SSA profile was then downsampled by averaging at the resolution of the density profile. Layer thicknesses used in numerical simulations are set to match the resolution of the density measurements, that is about 10 cm. The SSA and density profiles were then extended to 100 m depth by repeating the last 1 m of the measured profiles. This rough approximation has little impact at high frequencies because the altimetric signal usually comes from the upper part (above 5.8 m depth) where measurements were taken. However, at lower frequencies, in particular in the S band, the wave penetration depth may exceed 8 m. To evaluate the possible impact, we used a snowpack measured up to 20 m depth on the central Plateau (76°37' S / 117° 55' E). This latter site was not used in this study because no roughness measurements were acquired. We compared the altimeter simulations driven with the 20 m deep snowpack and with the same snowpack cut at 8 m and extrapolated as described in the method. The difference of stratification between 8 m and 20 m deep induces a maximal bias in interface contributions of 2% in the S-band, and the impact on the waveform shape is reasonably weak.

Figure 3 illustrates density and SSA profiles for ago5^E (on the EAIIST traverse) and stop2^A (on the ASUMA traverse). The mean SSA and density of each site are given in Table 1. Overall, the two southernmost snowpacks sampled during EAIIST are more stratified, less dense and have a lower SSA (i.e. bigger snow grains) compared to those acquired on the ASUMA area. They feature higher density variations owing to a lower accumulation rate in the central Antarctic Plateau (Fig. 3).

The snow temperature was measured with a Pt100 sensor located at the bottom of the drilled hole for a duration of 24 h. At this depth, the temperature is close to the annual mean temperature. For the simulations, the temperature profile was assumed uniform. The potential impact of temperature variations is investigated in Section 4.5 with simulations using seasonal temperatures (e.g. June-July and December-January average) recovered from the daily time series of surface temperatures of ERA5 data (Hersbach et al., 2020).

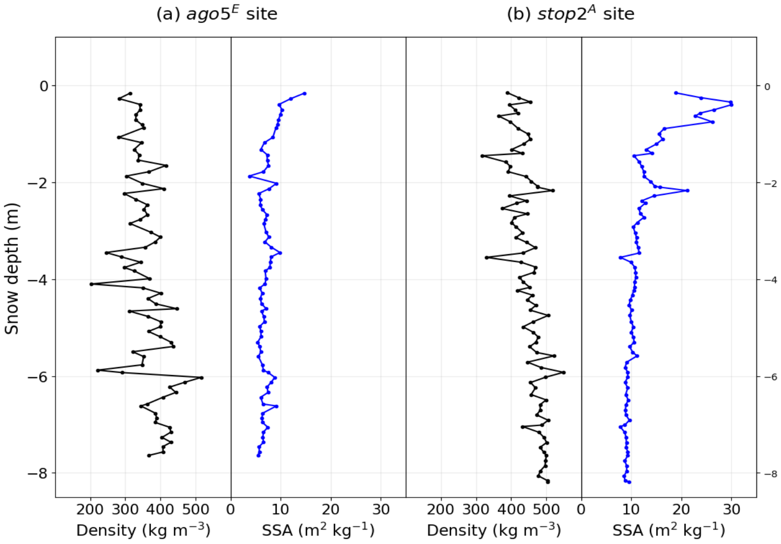

Figure 3: Density and SSA profiles measured at a) ago5^E (EAIIST traverse) and b) stop2^A (ASUMA traverse).

3.3. Measurements of the surface roughness

The surface roughness was modeled in SMRT using the GO approximation, which requires the Mean Square Slope of the surface (MSS) as input. To measure this parameter, Digital Elevation Models (DEM) were acquired in the field using a photogrammetry method. Because it is relatively new and provides a critical parameter, the full procedure is described hereafter.

3.3.1. Point cloud acquisitions

For each site, about 200 digital pictures were taken over an area of $\sim 10{\times}10\,\mathrm{m}^2$ for ASUMA sites, and $\sim 5{\times}5\,\mathrm{m}^2$ for EAIIST. A Canon EOS 5D digital camera (12-megapixel resolution) equipped with a filter selecting near-infrared wavelengths ($> 800\,\mathrm{nm}$) was used to enhance the contrast. The focus was set to infinity (Irvine-Fynn et al., 2014). Pictures were taken every $\sim 50\,\mathrm{cm}$, turning around the area, such that the overlap between two successive pictures is at least 30 %. The center of each picture was aligned with the center of the whole area, and the camera was far enough to capture a large zone. Three turns were performed to take pictures with three different angles, that is with the camera at 1 m from the ground, 1.6 m (eye level), and 2 m using a metal arm. These variations of angle prevent the doming effect (Smith and Vericat, 2015, Smith et al., 2016, Gharechelou et al., 2018).

At least 10 identifiable targets were placed within the area prior to the picture acquisition, and georeferenced afterwards using a Differential Global Positioning System (DGPS). Accurate geographic coordinates of the targets were measured using GNSS dual-frequency multi-channel Leica DGPS receivers. For this, a base station was set up near the area and the roving antenna was placed exactly above the target center with a given constant vertical offset (15 cm). Given a baseline generally not exceeding 50 m, carrier phase Real-Time Kinematic (RTK) positions have a theoretical relative horizontal and vertical accuracy of respectively 1.0 and 1.5 cm. An extra error term arises from improper positioning (offsets and tilting) of the roving antenna over the target which is estimated around 2 to 3 cm leading to a maximum square root global error of

3.5 cm. Half of the targets are used as control points to constrain the dense point cloud construction and the other half as reference points for estimating the errors. At least one target was positioned close to the lowest part of the area, and another one close to the highest part so as to cover the full vertical range of heights.

The pictures were processed using the recommended workflow of Agisoft Metashape Professional 1.6.2 software (Agisoft, 2019) to create point clouds. The spatial resolution of the DEM was 3 cm and the absolute error estimates of position targets with the checkpoints were lower than 2 cm for all sites.

The result of this protocol and processing was a non-uniformly distributed set of millions of points for each site.

3.3.2. MSS estimation

To compute the MSS from the irregular point cloud, four steps were followed:

- The point cloud is interpolated and aggregated on a regular grid with 3 cm spacing. Each grid-cell without elevation value is masked.

- The cloud is detrended by subtracting the least square regression plane from the original cloud.

- The detrended point cloud is smoothed to remove noise with a local averaging 3×3 window. The final spatial resolution becomes 9 cm.

- The MSS is calculated as the mean square of the slopes of the elementary surfaces composing the DEM following the definition of Belem et al. (2000).

The measured MSS are given for each site in Table 1. Considering all sites, the average MSS is equal to 0.02 ± 0.01. The local standard deviation estimated for stop5^A where two nearby areas were sampled is 0.005, which is small compared to the overall MSS. It suggests that a good representativeness of the local MSS is obtained with two nearby sampled areas. The mean MSS measured for ASUMA sites is higher (0.03) compared to the mean MSS of the EAIIST sites (0.01). Legresy et al. (2005) also observed larger surface roughness features close to the coast than on the central Plateau, probably due to the presence of stronger katabatic winds. To the best of our knowledge, this is the first in-situ

MSS measurements at centimeter-scales over the Antarctic Plateau covering a large latitudinal range. To give an order of magnitude, the MSS is usually below 0.03 over an oceanic surface when the wind speed is lower than $10\,\mathrm{m\,s^{-1}}$. It increases quickly with increasing wind speeds (Li et al., 2013).

3.4. Altimeter observations

Several time-series of nadir-looking pulse-limited altimeter observations have been collected.

For the Ku band (13.575 GHz, 2.3 cm wavelength) and the S band (3.2 GHz, 9.3 cm wavelength), the ENVISAT dual-frequency radar altimeter observations were downloaded for the period September 2002 to December 2007 (S band) and to October 2010 (Ku band) from the ESA website, using the Envisat Altimetry Full Mission Reprocessing V3.0 dataset (https://earth.esa.int/, last access: October 2020). Acquisitions were performed at an altitude of about 800 km every 330 m along-track on a 35-day repeat cycle orbit (Zelli and Aerospazio, 1999). The time record is 400 ns, sampled at $\Delta t = 3.125$ ns (equivalent to about 47 cm vertical resolution) for the Ku band and at $\Delta t = 6.25$ ns (94 cm vertical resolution) for the S band. The antenna 3 dB beamwidth is 1.35° in the Ku band and 5.5° in the S band. The ground footprint is about 15 km in diameter (Schwegmann et al., 2016).

Observations from the Sentinel-3A SRAL instrument were collected in the Ku band, covering the period July 2016 to December 2017. Sentinel-3A observations were processed at CLS (Collecte Localisation Satellites) with the CNES Sentinel-3 Processing Prototype (S3PP) which performs level 1 and level 2 processing. In contrast to ENIVSAT, Sentinel-3A operates in a high along-track resolution mode (SAR altimetry mode). For this study, data pulses were processed in the conventional way at level 1, in pseudo-LRM, using the CNES S3PP algorithm (Yang and Zhang, 2019), which makes it suitable for the comparison with SMRT simulations. Sentinel-3A has a repeat cycle orbit of 27 days and an altitude of about 814 km. The time record in pseudo-LRM and the 3 dB beamwidth antenna are the same as those of ENVISAT in the Ku band.

For the Ka band (35.75 GHz, wavelength 0.8 cm), the SARAL-AltiKa altimeter observations were downloaded for the period March 2013 to December 2018 from the CNES data center, using the GDR-T version (https://aviso-data-center.cnes.fr/, last access: October 2020). The Indian-French SARAL-AltiKa mission has a 35-day repeat cycle orbit with the same altitude as ENVISAT. The time record is sampled at $\Delta t = 2.08\,\mathrm{ns}$ (31 cm vertical resolution). The antenna 3 dB beamwidth is 0.605°, resulting in a footprint on the ground of about 8 km diameter (Verron et al., 2015).

All the collected observations are at level 2, and are corrected for atmospheric and geophysical effects (Rosmorduc et al., 2011).The satellite does not scan the same position at each pass exactly. This is therefore advisable to take an average of several consecutive waveforms over a similar surface (Yi and Bentley, 1994). This process of averaging is necessary to reduce the effect of irregular waveform shapes. All the observations acquired within a maximal distance of 2 km from each site were selected. 2 km was chosen as a trade-off in order to 1) get enough observations to compute average and filter noise, and 2) minimize topographic variations within the footprints which may greatly impact the shape of the waveform. Only the waveforms that had the same leading-edge position in the analysis window were kept (i.e. with a tolerance of ± 1 gate around the mean position). Indeed, due to the local heterogeneity of the surface within the 2 km radius (topography and sastrugi), the measured waveform is not necessarily positioned at the nominal tracking gate in the window analysis (gate 44 for Sentinel-3A for instance) and can drift around this nominal position (Brenner et al., 1983). After this selection, only sites with at least 50 waveforms were kept for the analysis. The waveforms from November to January months were then averaged for each site to build what is further referred to as the observed waveform. With this averaging, we assume that the impact of the spatial variability of snow properties over a 2 km radius area on the waveform shape is negligible and that the snow properties measured locally well represent the snowpack in the sensor footprint. Moreover, we used an observed waveform averaged over the summer season because due to the 35-day cycle of satellite orbits there are no enough altimeter observations acquired at the same period as the in-situ measurements. Adodo et al. (2018) estimate waveform amplitude variations of 0.1, 0.2, and 0.3 dB in the Ka, Ku, and S bands, respectively, for the summer period which is much lower than the model performance.

3.5. Simulations and evaluation

3.5.1. Simulation framework

For a first verification, SMRT was compared to the L08 model (Lacroix et al., 2008a). For a fair comparison, SMRT was configured so as to match the particular configuration implemented in L08. However, it is important to stress that this L08 configuration is not the one we recommend to use with SMRT, and it was not used for the comparison with the satellite observations as presented in the next sections.

The snowpack used for the comparison with L08 is the same as the one used in (Lacroix et al., 2008a) and aims at representing snow conditions at the surface of the Vostok Lake. In practice, this snowpack is a synthetic snowpack based on scattered information and measurements representative of the Antarctic Plateau. The snow grain size is uniform and equal to 0.9 mm, and the surface snow density is $240\,\mathrm{kg\,m^3}$. For L08 simulations, 1) the snow microstructure is represented as an ensemble of independent penetrable spheres, an option available in SMRT (Picard et al., 2018), 2) The electromagnetic theory follows the original IBA theory (Mätzler, 1998) and the relative dielectric constant of ice is estimated using Tiuri et al. (1984), 3) the IEM theory (Fung et al., 1992) is applied to compute the rough surface scattering considering the millimeter-scale surface roughness of the L08 synthetic snowpack, and 4) L08 assumes that the phase function $P(0, 0, \pi, z)$ is independent of the angles and is therefore equal to the scattering coefficient κ_s. This latter rough approximation was implemented in SMRT for the sole purpose of this L08 comparison. We also checked that the same sensor configurations were applied using the ENVISAT sensor in the Ku and S bands. Moreover, the L08 and SMRT models use different analytical expression of the transmitted power P_t: L08 represents the P_t with a cardinal sinus with a width of 0.886 Δ gate (at -3 dB), while SMRT models the P_t with a Gaussian approximation (see Eq. 5). Because of this slight difference and in order to guarantee the same configuration, we ran the L08 and SMRT simulations without the convolution with the P_t. This is acceptable for this first analysis aiming at verifying the similarity between both models.

For the full assessment of SMRT with the altimeter observations, the multilayered snowpack was prescribed using the in-situ measurements and following Picard and Fily (2014). Snow density, SSA, temperature, MSS, terrain slope and σ_{surf} were directly given as inputs. Following Picard et al. (2009), the atmospheric contribution was neglected. SMRT was run with the IBA theory (Mätzler, 1998) to compute volume scattering. The snow microstructure was represented by a collection of non-penetrable spheres (a.k.a Hard Sphere model) with a radius equal to the optical snow grain radius r_{opt}. This variable was related to SSA measurements by $r_{\mathrm{opt}} = \frac{3}{SSA\rho_{ice}}$,with $\rho_{ice} = 917\,\mathrm{kg\,m^{-3}}$. However, several studies have shown that this representation was insufficient to properly describe the real snow microstructure (Roy et al., 2013, Picard et al., 2014, Vargel et al., 2020). Although several approaches are available to overcome this problem, they are relatively equivalent (Picard et al., 2018). Here we applied a simple scaling factor of 2.3 on r_{opt} based on measurements acquired in Antarctica at the Concordia research station in the central Plateau (Picard et al., 2014).

SMRT was run with the GO approximation for surface and interface backscattering calculation. The GO was chosen instead of IEM because the roughness rms heights estimated from the in-situ DEM were larger than 10 cm, which falls in the validity domain of GO but not of IEM at the studied frequencies. However, the choice of the GO approximation involves several assumptions. The GO approximation is only valid when the roughness features have a size close to or larger than the incident radar wavelengths, i.e. above 0.8, 2.3, and 9.4 cm for the Ka, Ku, and S bands, respectively. Here we assume that the roughness horizontal scale above 10 cm is sufficiently large compared to the S band wavelength. Moreover, GO assumes scattering on the facet is specular for all studied wavelengths. Multi-scale roughness models have not been considered because we had no way to characterize the sub-centimeter scales in the field. The limitations of these two assumptions are discussed further.

Also, in our simulations we assume that the roughness of the buried interfaces is similar to that of the surface, i.e. characterized with the same input MSS. In reality, the roughness of buried interfaces may decrease with the snow compaction/accumulation, but such internal roughness measurements at centimeter scales have not been carried out to our knowledge. SMRT can run with a different MSS value for each interface and the waveform sensitivity to different roughnesses is further discussed by running SMRT with varied MSS values of the internal interfaces when the surface MSS is fixed.

To summarise, the different assumptions made to assess radar waveforms simulated in LRM mode with SMRT are i) there is no multiple scattering; ii) the ice grains are spherical; iii) the considered roughness scale (above 9 cm) is sufficiently large compared to incident radar wavelengths; iv) the roughness at scales below 9 cm is smooth; v) the firm is composed with multiple homogeneous layers that have the same roughness; vi) surface scattering is independent of frequency; vii) the wave polarization is neglected for volume scattering due to the near nadir approximation; viii) the off-nadir effect is negligible; ix) the impact of temperature variations in the snow profile on the waveform shape is negligible; x) the impact of temporal variations of snow properties during the summer period on the waveform shape is negligible.

For the outputs, the total radar waveforms were modeled considering the convolution with P_{FIR}, P_t and the *pdf* (Eq. 2) to be compared with satellite observations.

3.5.2. Waveform parameters

The normalized simulated radar waveforms were compared for each site and each frequency with observed waveforms. The comparison was performed on the relative power to avoid the unknown biases impacting the observed waveform amplitudes (Legresy et al., 2005). More precisely, a constant normalization factor $\alpha(\nu)$ was estimated for each sensor and applied to the simulated waveforms for all sites. $\alpha(\nu)$ was calculated with the least-square regression of the simulated and observed waveform amplitudes. An explicit expression for $\alpha(\nu)$ is:

$$\alpha(\nu) = \frac{\sum_i A^{\mathrm{obs}}_{i,\nu} A^{\mathrm{sim}}_{i,\nu} - \sum_i A^{\mathrm{obs}}_{i,\nu} \sum_i A^{\mathrm{sim}}_{i,\nu}}{\sum_i (A^{\mathrm{obs}}_{i,\nu})^2 - (\sum_i A^{\mathrm{obs}}_{i,\nu})^2} \tag{17}$$

where $A^{\mathrm{obs}}_{i,\nu}$ and $A^{\mathrm{sim}}_{i,\nu}$ denote the observed and simulated waveform amplitudes, respectively, estimated with the ICE-1 retracking algorithm as follows (Wingham et al., 1986):

$$A_{i,\nu} = \sqrt{\frac{\overline{P_{r,i,\nu}(t)^4}}{\overline{P_{r,i,\nu}(t)^2}}} \tag{18}$$

where $\overline{P_{r,i,\nu}(t)}$ is the mean waveform for the site i at the frequency ν. A single constant normalization factor $\alpha(\nu)$ was computed for all sites at a given frequency, and was then applied to simulated waveforms to get the normalized simulated waveforms. The total backscattering coefficient σ^0 was estimated as the amplitude (Eq. 18) converted in dB.

The biases of surface elevations due to the wave penetration in the ice sheet were also investigated. Commonly used retracker algorithms estimate the ice sheet elevation with the midpoint of the leading edge of the observed waveform, which combines both surface and volume echoes. By separating each contribution, SMRT makes it possible to estimate the mean surface as if the snow was not transparent, by applying the retracked on the surface echo only. Here, the penetration elevation bias is the distance between the position of the midpoint of the leading edge of the total simulated echo (LEP_{TOT}) and the midpoint of the leading edge of the surface echo (LEP_{surf}), as proposed by (Yi and Bentley, 1994). LEP positions are estimated at 50% of the amplitudes estimated with Eq. 18. The precise quantification of other waveform parameters defined in the ICE-2 retracking algorithm of Legrésy and Rémy (1997) are out of the scope of this study and left for further work.

3.5.3. Penetration depth of the wave

To investigate the penetration depth impacting the radar wave, additional SMRT simulations were run without the convolution of P_{FIR}, P_t and the *pdf* to output the total backscattering intensity in the snowpack ($I_{\mathrm{tot}} = I_{\mathrm{vol}} + I_{\mathrm{int}}$). As for the total waveform, I_{tot} was provided as a function of altimeter gates g (or time). Here the wave penetration depth was estimated as the depth from the surface to the point corresponding to the center of gravity of the distributed backscattering intensity ('the EGC point'). It is further referred to as the depth of the echo gravity center 'd_{EGC}'. To estimate the d_{EGC}, the EGC gate was estimated as follows:

$$g_{\mathrm{EGC}} = \sum_{g=1}^{G} \frac{g I_{\mathrm{tot,g}}^2}{I_{\mathrm{tot,g}}^2} - LEP_{\mathrm{surf}} \tag{19}$$

The d_{EGC} was then deduced from g_{EGC}, Δt and the effective light speed in every layer.

Note that d_{EGC} differs from the 'e-folding depth' ('δ_{p}' in **?**) - which is the depth where the downwelling intensity of a radar wave is attenuated by 1/e, or the depth at which the optical thickness has reached 1 (Ulaby et al., 1986, Marks and King, 2014, Gay and Ferro-Famil, 2016). δ_{p} indicates the maximum penetration depth that can contribute to the backscattering coefficient considering snowpack properties and was calculated for each site to make a qualitative comparison with previous studies. However, d_{EGC} accounts for the vertical penetration measured by the e-folding depth and the horizontal spread of the waves (which depends on the altimeter antenna parameters) and is more representative of the depth which contributes to the radar altimetric signal.

Both d_{EGC} and δ_{p} parameters are controlled by the extinction coefficient κ_e in the snowpack which is the sum of the scattering and absorption coefficients (κ_s and κ_a, respectively). Therefore, κ_s and κ_a were computed with SMRT and analyzed for each frequency and snowpack to investigate the penetration depth sensitivity to snowpack properties.

4. Results

SMRT waveforms are first compared to L08's simulations in Section 4.1. The performance of SMRT is then evaluated with real observations in Section 4.2. The sensitivity of the waveform shape and elevation bias to the snowpack properties is investigated in Section 4.3. The assessment of simulations obtained with fitted MSS values is analyzed in Section 4.5. The influence of the snowpack properties on the penetration depth of the wave is finally studied in Section 4.6.

4.1. Comparison with L08

Figure 4 shows the comparison between SMRT and L08 simulations. Overall, SMRT simulations agree with L08 simulations within 1.7% and 1.4% Root Mean Square (RMS) in the Ku and S bands, respectively. Such a good agreement supports the correctness of the SMRT extension. The small residual differences are mainly due to the calculation of the imaginary part of the ice permittivity (ϵ_i'') according to snow temperature. L08 uses a different formulation (Matsuoka et al. (1996) v.s. Tiuri et al. (1984)). ϵ_i'' is involved in the computation of the losses by absorption in the snowpack (κ_a). The simulations are more impacted by this difference in the S band than in the Ku band because the absorption plays a stronger role than scattering at lower frequency.

The comparison between the maximum of the simulated waveform of the surface echo and the total echo shows that the leading-edge width is wider, by about 10 ns in the Ku band due to the wave penetration in the snowpack (Fig. 4a). In the S band, the total echo is even more delayed since the wave penetrates deeper at lower frequency. At this frequency, there is no distinct maximum of the simulated waveform of the total echo because the signal still penetrates in (and is reflected by) the snowpack even after 400 ns (size of the analysis window, see Fig. 4b).

L08 and SMRT simulations not only agree for the total returned power but also for the surface and volume components, at both Ku and S bands (Fig. 4). Here, the volume echo comes from scattering by snow grains only since the input

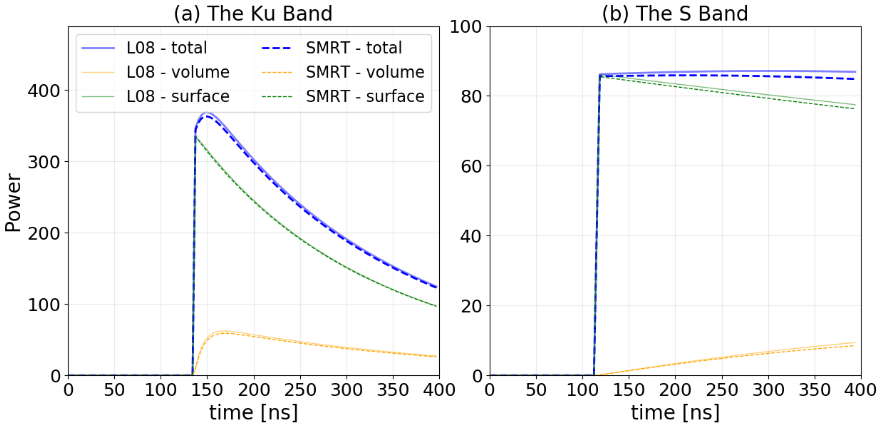

Figure 4: Simulated waveform at the Vostok Lake with SMRT (dotted lines) and L08 (full lines) in a) the Ku band, and b) the S band, comprising the total return power (blue), the return power from the surface (green) and that from the snow grains (orange).

synthetic snowpack has no internal density discontinuity, implying no internal interface echo. Note that the beginning of the leading-edge is exaggeratedly straight here, because the convolution with P_t was disabled for the purpose of the comparison as discussed previously.

4.2. Evaluation of the backscattering coefficient

Figure 5 shows the total backscattering coefficient σ^0 calculated with the ICE-1 retracker for the normalized simulated waveforms and from averaged observed waveforms for each site and for all sensors. The values span a range of 10 dB approximately. The overall absence of bias between the simulations and the observations is a consequence of the normalization applied on the simulated waveforms, and can not inform us about the model skills. In contrast, the inter-site variations can be safely interpreted and the good alignment with the first diagonal indicates strong model skills. This is confirmed by the high Pearson correlation coefficients of 0.96, 0.79, 0.85, and 0.99 in the Ka band, the Ku band of both ENVISAT and the Sentinel-3A and the S band of ENVISAT, respectively.

The model is also able to predict the marked difference observed between EAIIST and ASUMA sites, about 4 dB, at all frequencies. This difference can be explained by the spatial gradient of surface roughness observed from the coast (highest measured MSS) to the interior (lowest MSS, Table 1). A rough surface tends to reflect less energy in the backward direction than a smooth surface due to the tilted facets of the surface. This induces a lower backscattering coefficient from the surface. However, other properties of the snowpack which also vary in space may participate to this pattern, such as the snow grain size, temperature, and density. This point is discussed further in Section 4.5.

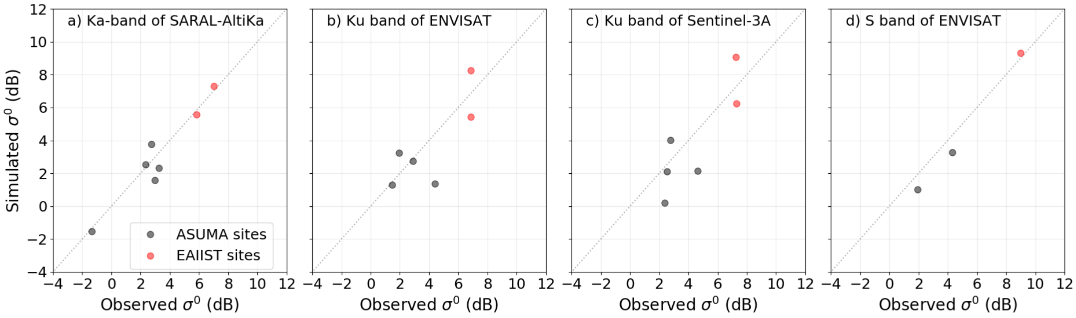

Figure 5: Observed and simulated σ^0 estimated with the ICE-1 retracker for the EAIIST sites (red) and the ASUMA sites (grey).

4.3. Qualitative evaluation of the waveform shapes

Figure 6 shows the simulated and observed waveforms for each site for all sensors. The observations of ENVISAT and Sentinel-3A are distinguished. The missing plots correspond to the sites with less than 50 valid observations (Section 3.4). Figure 7 shows the relative contributions from the surface, snow grains, and internal interfaces to the total return power for each site and sensor configuration using the whole waveform shape.

Overall, SMRT simulations represent the waveform shapes well for all sensors by considering the convolution with the P_{FIR}, P_t and pdf. The penetration of the wave within the snowpack causes a time delay visible on the upper part

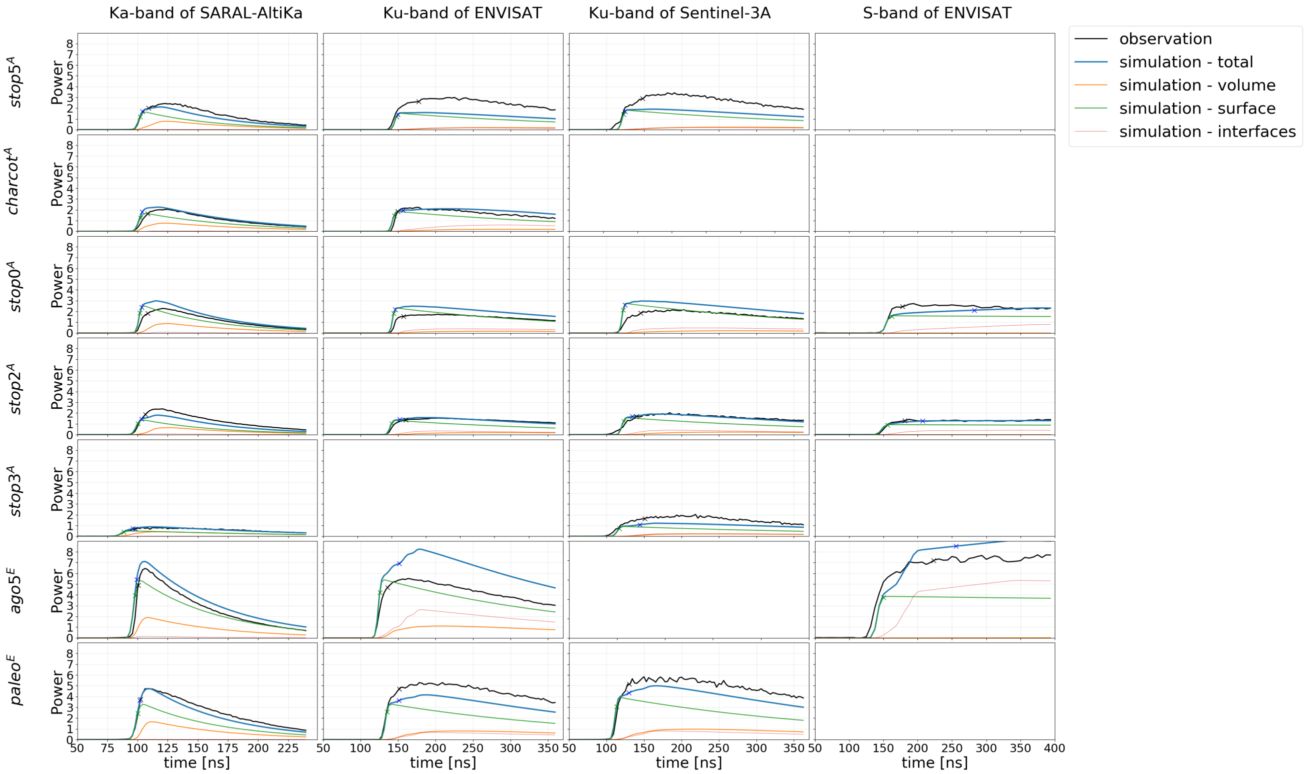

Figure 6: Observations (black lines) and simulations (blue lines) of waveforms at the 7 sites with the SARAL-AltiKa sensor in the Ka band (first column), ENVISAT in the Ku band (second column), Sentinel-3A in the Ku band (third column), and ENVISAT in the S band (fourth column). The volume, surface, and internal interface contributions to the simulated total echo are shown (in orange, green and red, respectively). The waveform amplitudes are indicated for the total observed and simulated waveforms (dark and blue crosses, respectively) and simulated surface echoes (green crosses). The empty boxes correspond to the sites not reaching 50 valid observed waveforms over the summer period for a given sensor and band.

of the waveform leading-edge, which leads to a more rounded shape compared to the classical waveforms observed when only the surface echo is present and the surface is flat. This delay is well taken into account with SMRT in the Ka band, and the position of the waveform amplitude is similar for simulations and observations, as highlighted with the crosses in Fig. 6. In the Ka band, the delay is shorter for EAIIST sites than for ASUMA sites, with thinner leading-

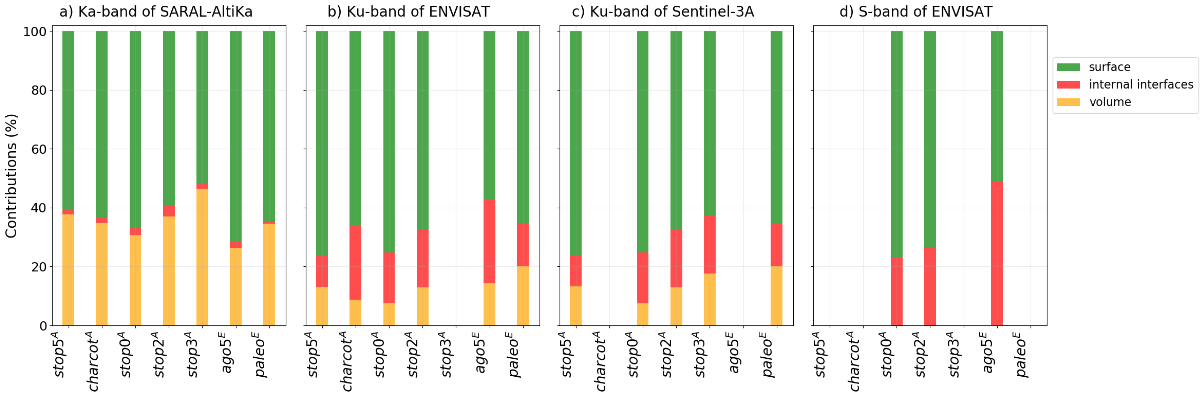

Figure 7: Percentage of contributions of echoes from the surface, the volume (snow grains) and the internal interfaces to the total return power simulated with SMRT. Contributions are estimated using the whole total waveform shape.

edge widths, which suggests a smaller penetration depth of the wave towards the interior of the continent. At lower frequencies, the waveform increases slightly slower than at high frequencies (Ka-band) near the maximum and decreases less abruptly due to the deeper wave penetration in the snowpack. This frequency-dependent delay is simulated with SMRT (Fig. 6). The position of the waveform maximum amplitude is more scattered in the Ku-S bands than in the Ka band but overall the position is better simulated when taking into account the echo from both the surface and subsurface (blue crosses in Fig. 6) compared to that solely arising from the surface (green crosses).

A lower waveform amplitude is observed for ASUMA sites compared to EAIIST sites (Fig. 6). Both observed and simulated waveforms feature the lowest amplitude at stop3^A and the highest at ago5^E for all sensor configurations. As for σ^0, a small amplitude is an indicator of a rough surface. Also, the surface slope shifts the Point of Closest Approach (POCA) from the nadir and greatly decreases the backscattered energy when the slopes are larger than the antenna aperture (Legresy et al., 2005). In this study, the two steepest sites are charcot^A and stop3^A in the ASUMA area, and indeed have the lowest observed and simulated waveform amplitudes (Fig 6). The small biases between the observations and simulations obtained at stop0^A, ago5^E, and paleo^E in the Ku band (both for ENVISAT and Sentinel-3A sensors) are probably caused by the difference between the local in-situ measurements used to drive SMRT (density, SSA, temperature, roughness) and what the average over the sensor footprint. In particular, for ago5^E SMRT overestimates both the amplitude and the leading-edge of the waveform compared to the observation (Fig. 6). For this site, Fig. 7b shows that the contribution of the internal interfaces is particularly high (≥ 30 %), which is caused by particularly large variations of measured density, visible in the profile shown in Fig. 3, that may not reflect the average stratification of the snowpack as seen by the satellite sensor. This is why even with in-situ measurements, these input snow parameters probably need to be fitted to get effective values closer to what is seen at a larger scale. This point is further analyzed in Section 4.5.

Figure 7 shows that the surface has the main contribution for all sites and for all sensor configurations (~ 60 %, Fig. 7). In the Ka band, the surface contribution inversely varies with the measured roughness size (MSS). For instance, the small MSS measured at ago5^E (0.01) induces a high surface contribution (70%), while the high MSS measured at stop3^A (0.05) results in a relatively low surface contribution (53%, Fig. 7a). This result highlights that SMRT correctly takes into account the high impact of the surface roughness on the total returned power. Moreover, while the thinner leading-edge width of the EAIIST sites suggests a smaller penetration depth in the Ka band (Fig. 6), the volume contribution simulated for EAIIST sites is of the same order of magnitude as that of ASUMA sites (Fig. 7a). This is due to the coarser snow grains on EAIIST compared to ASUMA (Table 1), leading to higher volume scattering. In practice, the volume contribution is even much larger for EAIIST sites, as shown by volume echo amplitudes in Fig. 6 in the Ka band, but in Fig. 7a the surface contribution of EAIIST sites is very high due to the smooth surface. In the Ka band, the volume echo represents ~ 40 % of the total returned power, while the contribution of the internal interfaces is negligible (Fig. 7a). In the Ku band, the contribution of snow grains decreases to about 20 %, while the

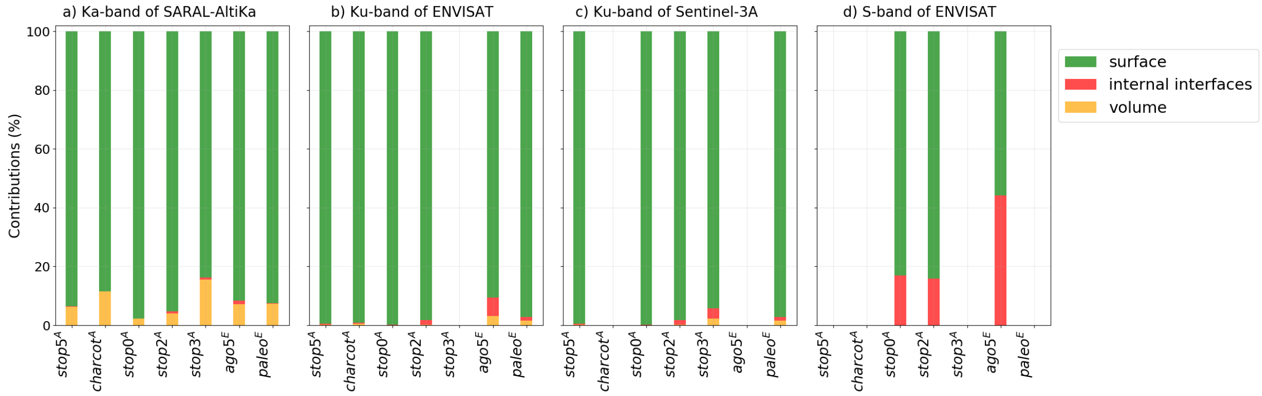

Figure 8: Percentage of contributions of echoes from the surface, the volume (snow grains) and the internal interfaces to the total return power simulated with SMRT. Contributions are estimated on the leading-edge portion of the total waveform.

one from the interfaces increases to 13 % of the total echo (Fig. 7b). In the S band, there is virtually no volume scattering (Fig. 7d) because the snow grains are very small compared to the wavelength ($<1\,\mathrm{mm}$ versus $\sim 9\,\mathrm{cm}$ wavelength). Conversely, the contribution of the interfaces increases, enhanced by the deeper penetration of the wave. The contribution of the interfaces is twice as low for the ASUMA sites (25% of the total echo) as for ago5^E (50% of the total echo). This is due to the very rapid density variations measured at ago5^E (Fig. 3), which increases the internal reflections.

Contributions were also calculated for the leading-edge part, i.e. portion of the waveform before the maximum amplitude (Figure 8). Results illustrate that: 1) in the Ka band, only the surface and volume contributions impact the leading-edge - and the volume contribution is relatively weak with only 10%; 2) In the Ku band, only the surface contribution impacts the leading-edge of the total echo (up to 98%), except for ago5^E where the uppermost layer is composed of many thin layers and the density contrasts in the topmost part of the snowpack lead to a contribution from the internal interfaces equal to 8%; 3) In the S band, only the surface and interface contributions impact the leading edge.

Similar results are obtained for ENVISAT and Sentinel-3A observations in the Ku band. Noting that the ENVISAT observations were acquired a few years before those of Sentinel-3A (2002 to 2010 vs 2016 to 2017) confirms that the snowpack is fairly stable over a few years. Using altimeter observations acquired far back in time from in-situ measurements is likely not an issue on the Antarctic plateau, at least less of a problem here compared to other snow-covered regions in the world. Given the similarities between both sensors in the Ku band, only the analysis with ENVISAT is detailed in the following.

To conclude, the qualitative analysis of waveforms highlights that for the three frequencies the sites in the central Plateau (EAIIST) have higher amplitudes compared to sites closer to the coast (ASUMA) and this pattern is reproduced by the model. The simulations represent the waveform shapes well (leading-edge, amplitudes, slopes after the leading-edge) except in a few cases. In the Ka band, the thin leading-edge width for EAIIST sites (i.e. southernmost sites) indicates a shallower wave penetration compared to that close to the coast, but not necessarily sites with a lower volume contribution since snow grain sizes are larger in the central Plateau. The surface contribution is the main contribution of all sensor configurations but it strongly depends on surface roughness, which is smaller on the central Plateau. The impact of volume scattering increases with increasing frequency (up to 40% of the total echo in the Ka band), while the impact of internal interface reflections increases with decreasing frequency.

4.4. The elevation bias

For all sites, the mean elevation biases due to the wave penetration are 12.8 ± 7.1 cm, and 15.6 ± 7.2 cm in the Ka and Ku bands, respectively. This is an important bias that can have a strong impact in mass balance studies for the Antarctic ice sheet given that the snow accumulation rate is less than a few centimeters per year in the interior of the continent and a few tens of centimeters near the coast (Rémy and Parouty, 2009, Vaughan et al., 1999).

stop3^A appears as an extreme case with the strongest elevation bias compared to the other sites. This is probably due to an indirect effect of the slope that impacts the surface/volume contributions. stop3^A has the largest slope value (0.21°, Table 1) and in presence of large slopes, the point of impact from the nadir is shifted so the former echo amplitude is decreased compared to the latter echoes (Lacroix et al., 2008a). The consequence is a change in the leading edge width and in the slope after the leading edge of the waveform compared to that of a flat surface. A sensitivity analysis of the elevation bias to slope uncertainties was performed by varying slopes with a constant error of ± 0.1° for each site and sensor (not shown), and the elevation bias appeared to be insensitive to slope errors for sites having a slope below 0.2°. This topographic effect is discussed further in Section 5, and here to only analyze the elevation bias due to the volume effect we only consider the sites with a small slope (below 0.2°).

Excluding stop3^A, the elevation bias is spatially homogeneous in the Ka band and equal to 10.0±2.3 cm close to the coast (ASUMA sites), and 10.5±2.0 cm in the central Plateau (EAIIST sites). It means that the differences of snowpack properties within our dataset have a negligible impact on the leading edge, and therefore on the elevation bias retrievals. In contrast, in the Ku band, the elevation bias has a mean value of 10.6±3.6 cm close to the coast (ASUMA sites), and 21.2±4.0 cm, in the central Plateau (EAIIST sites), a two-fold difference between both regions. As shown in Figure 7b the snowpack contributions (from both internal interfaces and snow grains) are larger in the central Plateau than closer to the coast which causes a twice larger time delay on the upper part of the waveform leading-edge compared to close to the coast, which explains the two-fold elevation bias. Several parameters play a role in this spatial difference. In particular, the lower accumulation rate in the interior of the continent results in bigger snow grains - and increased volume echo - and stronger density contrasts with thinner layers which increase the internal reflections (Legrésy and Rémy, 1997). In the following section, a sensitivity analysis is conducted to better understand the impact of snowpack properties on the waveform shape.

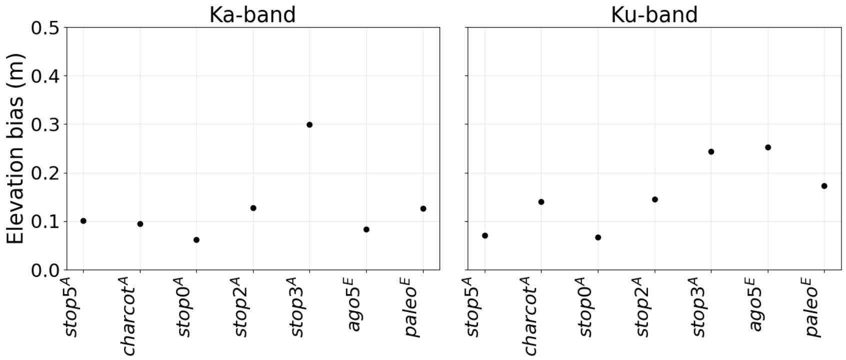

Figure 9: Elevation biases estimated in the Ka and Ku bands (a, b), simulated with for all sites.

4.5. Sensitivity analysis

The performance of the model depends on the snowpack given as input, which is measured at one local point and may not be representative of the sensor footprint (> 4 km). To investigate the potential impact of snowpack uncertainties, SMRT simulations are computed for all sites and sensor configurations by varying successively MSS by ± 20% of the initial measurements, the SSA and density by ± 20% over the entire profiles, and snow temperature from the mean summer temperature (December–January) to the mean winter temperature (June–July) retrieved from ERA5. This sensitivity analysis concerns the sites with a slope below 0.2° and the topographic effects are assumed to be weak enough not to disturb the waveforms (see Table 1). As we obtained similar results for all sites with a slope below 0.2° (i.e. all sites except stop3^A), we present the stop2^A results here only. Figure 10 shows the waveform shapes obtained by varying the MSS, SSA, density, and temperature.

4.5.1. Sensitivity to surface roughness

A change in MSS has a slightly larger impact at lower frequencies, as shown in Fig. 10a, 10e and 10i. With a decrease of 20% of the measured MSS at stop2^A (from ~ 0.03 to ~ 0.024), the waveform amplitude increases by 16 %, 22% and 25% in the Ka, Ku, and S bands respectively, and an increase of 20 % of MSS

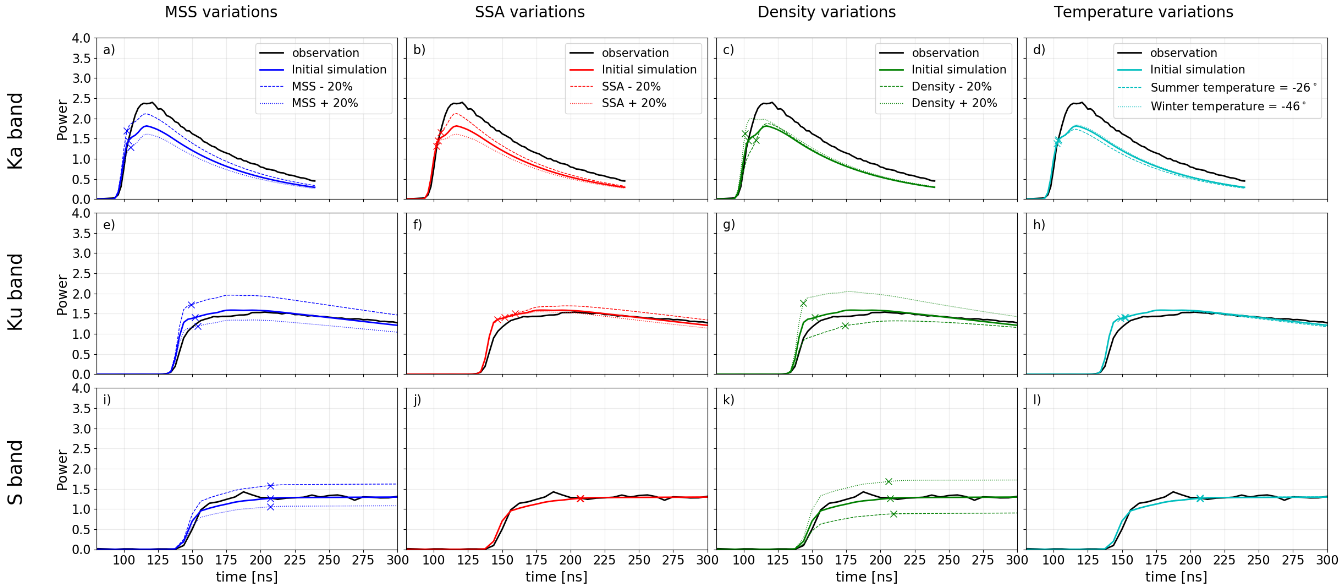

Figure 10: Waveform variations at stop2^A with MSS variations of ± 20% in simulations (first column); with SSA variations of ± 20% (second column); with density variations of ± 20% (third column); with temperature variations from the mean summer temperature (December and January) to the mean winter temperature (June and July) (fourth column). The slope of the stop2^A site is of 0.15°. Results are given for the Ka band of SARAL-AltiKa (first row), the Ku band of ENVISAT (second row) and the S band of ENVISAT (third row). Simulated waveform maximums are indicated with crosses.

(from ~ 0.03 to ~ 0.036) decreases the waveform amplitudes by 11 %, 15 % and 17 % in the Ka, Ku, and S bands respectively. These variations are a direct consequence of the varying contributions of the surface and interfaces compared to that of snow grains. It is not due to a change of surface scattering, because under the geometrical optics (which assumes a roughness scale much larger than the wavelength) the simulated surface scattering is independent of the frequency. The waveform amplitude decreases with a rougher surface because less energy is reflected directly to the sensor.

The leading-edge width (LeW) is weakly impacted by the MSS variations in the Ka and Ku bands, as shown by the waveform amplitude positions in Fig. 10a, e. As a result of the increase in the surface contribution, the waveform shape is sharper when the surface is smoother, which reduces the LeW (i.e. the elevation bias). For instance, for stop2^A we estimate that a MSS decrease of 20% features a decrease of 2 cm of the elevation bias retrieved from the Ka or Ku bands. Overall, MSS variations mainly impact the waveform amplitude - and so the σ_0 parameter - whilst the change in LeW is small.

4.5.2. Sensitivity to the SSA

The waveform sensitivity to SSA variations is larger at higher frequencies (Fig. 10b, 10f and 10j), because the variations of snow grain sizes only impact the volume scattering that is negligible at low frequency. For instance, by varying the SSA by ± 20%, the waveform amplitude varies by ± 10%, ± 6%, and ± 0.05% in the Ka, Ku, and S bands, respectively. Moreover, a decrease of SSA induces an increase in the simulated waveform amplitude. A lower SSA represents a larger optical radius r_{opt} implying more volume scattering by grains. A change in SSA thus modifies the surface and volume respective contributions at high frequencies, and so impacts the LeW as well as the slope after the LeW. In the Ka and Ku bands, a decrease of SSA has the effect of shifting forward the waveform leading-edge due to the higher volume contribution (Fig. 10b, f), and thus increases the elevation bias. For stop2^A we estimate that a decrease of 20% of SSA (i.e. from ~ 12.4 to $\sim 9.9\ \text{m}^{-2}\,\text{kg}^{-1}$) features to an increase of 2 and 3 cm of the elevation bias retrieved from the Ka and Ku bands, respectively. The impact in the S band is negligible, suggesting that the combination of the Ka and S bands should help to better characterize the contribution from snow grains. This is consistent with former studies of Guerreiro et al. (2016) and Guerreiro et al. (2017), except that in this latter, it is suggested to use the Ka and Ku bands to quantify the volume echo.

4.5.3. Sensitivity to snow density

The waveform sensitivity to snow density is stronger at lower frequencies with an amplitude increasing with a larger density (Figures 10c, 10g and 10k). The volume contribution is lower for a denser snowpack since the wave penetrates less deeply. However, this aspect is compensated by an increase of the surface and internal interface reflections due to density variations enhancing the dielectric contrast between the layers. At lower frequencies, the signal depending mainly on the surface and interface echoes, the waveforms are thereby more sensitive to density variations. With density variations of ± 20%, the amplitude varies by ± 5%, ± 18%, and 32% in the Ka, Ku, and S bands, respectively. Also, in the Ka and Ku bands, when the snowpack is denser near the surface, the waveform shape becomes sharper due to the larger surface scattering and the leading-edge is shorted as illustrated by the position of the waveform amplitudes (Fig. 10c, g). A change in near-surface density strongly impacts the elevation bias. For stop2^{A} we estimate that a decrease of 20% of density (i.e. from $\sim$ 449 to $\sim$ 359 $\mathrm{kg\,m^{-3}}$) features to an increase of 3 and 6 cm of the elevation bias retrieved from the Ka and Ku bands, respectively. The density is the most sensitive parameter impacting the LeW.

4.5.4. Sensitivity to snow temperature

The simulations considering snow temperature variations show a weak sensitivity to seasonal changes in the Ku and S bands when the snow temperature is considered uniform (Figures 10h and 10l). In the Ka band, the sensitivity is also low, and the waveform simulated with a higher temperature (-26° C as in summer) features a lower amplitude compared to the simulation with the mean annual temperature (-40.4° C). The temperature impacts the volume echo only, and this effect is due to the increase of the ice absorption at higher temperatures. This weak sensitivity of snow temperature variations shows that the seasonal changes of waveform amplitudes (i.e. σ_0) observed in previous studies (Adodo et al., 2018) are mainly due to SSA and density seasonal variations, rather than to snow temperature.

As a conclusion, this sensitivity analysis shows that in the Ku and S bands, there is a higher sensitivity of the waveform shape to the density and MSS than to SSA and temperature. In the Ka band, the MSS is the most sensitive parameter impacting the waveform amplitude, and therefore the σ_0. Moreover, the elevation bias is larger for 1) rougher surfaces, 2) larger grains, 3) less dense snows. On the central Plateau, the snowpack is smoother, less dense, and with larger grains than in the area close to the coast. In the Ka band, the estimated elevation biases for ASUMA and EAIIST are similar because of the combination of the three effects: on the central Plateau, the lower roughness tends to decrease the elevation bias while the lower density and SSA tend to increase the elevation bias, and this is the opposite pattern close to the coast. In the Ku band, the difference in density and SSA plays a more important role because the wave penetrates deeper. This is why the elevation bias is twice as high on EAIIST as on ASUMA.

4.6. Simulations with fitted MSS

Considering the high sensitivity to MSS on the σ_0 and the uncertainty associated with the local measurement of this parameter, we consider here the MSS as an unknown parameter. SMRT simulations are restarted and MSS values are fitted for each site by minimizing the deviation between the simulated and observed σ_0 at the three frequencies. The fitted MSS values are shown in Figure 11. They are in the ± 20 % range of the measured MSS values, except for stop5^A. The specific case of stop5^A, where the fitted MSS is 40% lower than the measured MSS (Fig. 11), suggests that the sampled area was particularly rough compared to the surrounding (sensor footprint of about 8-15 km in diameter in the Ku and Ka bands) and the representativeness of this measurement may be poor. The σ^0 retrieved with the ICE-1 retracker from the waveforms simulated using the fitted MSS have Pearson correlation coefficients of 0.97, 0.97, 0.99 in the Ka, Ku, and S bands, respectively (Figure 12). This is a significant improvement in the Ku band compared to the results obtained with the measured MSS (0.79). The quality of the model with the fitted MSS is better at low frequencies ($\leq$ 37 Ghz) since the wave penetrates deeper in the snowpack and is more sensitive to interface reflections - that depends on the interface roughness represented with the MSS - while in the Ka band the volume contributes to as much as 40% of the signal.

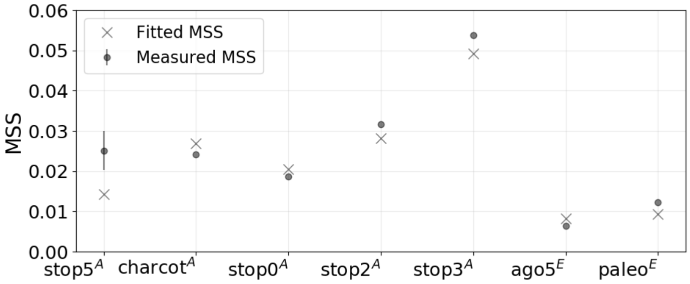

Figure 11: Measured (points) and fitted (crosses) Mean Square Slopes of the surface (MSS). Standard deviation at stop5^A represents the measured variability between the two nearby sampled areas.

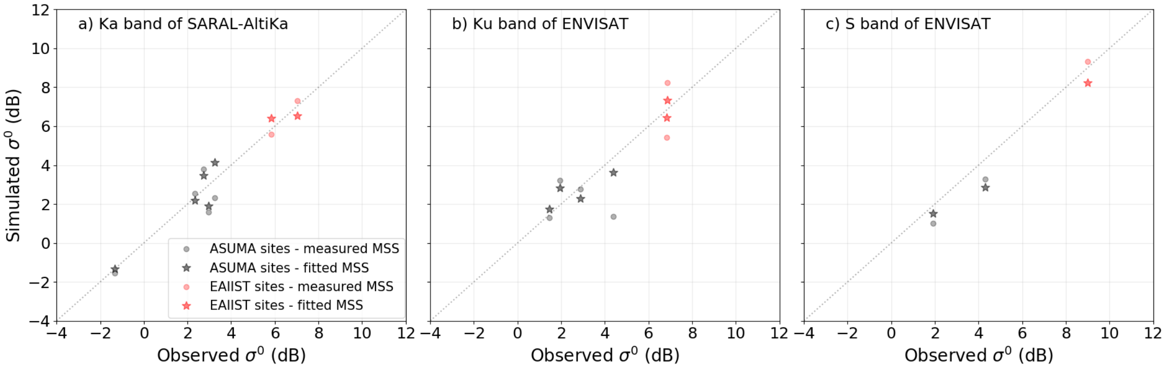

Figure 12: σ^0 in the Ka band, Ku, and S bands (a, b, c), simulated with measured MSS (points), and simulated with fitted MSS (stars).

Note that this fitted MSS value is not necessarily closer to the true value than the measurements because the optimization process can compensate for other unrelated sources of errors (SSA and density uncertainties), as shown in the previous section. Nevertheless, in the absence of surface roughness measurements, the fitted MSS of 0.03 in areas close to the coast and 0.01 in the interior of the continent appear to be a reasonable first guess to simulate surface scattering on the Antarctic ice sheet, with an uncertainty of the order of ± 20%.

4.7. Impact of snow properties on the wave penetration depth

We here investigate how the penetration depth of the wave is impacted by snow properties. Table 2 shows the depth of the echo gravity center (d_{EGC}) and the δ_{p} for all sites and three bands. The average d_{EGC} decreases from 0.9 ± 0.3 m to 0.3 ± 0.07 m in the Ka band from ASUMA to EAIIST areas and from 3.5 ± 0.9 m to 3.2 ± 0.003 m in the Ku band (Table 2). In contrast, in the S band, the average d_{EGC} increases from 3.7 ± 1.2 m to 5.8 m from ASUMA to EAIIST areas. A smaller d_{EGC} for the EAIIST area in the Ka and Ku bands indicates that the extinction κ_e is stronger in the central Plateau than it is closer to the coast, while the largest d_{EGC} in the S band suggests a lower κ_e in the central Plateau at low frequency.

Similarly, the mean δ_{p} decreases from 1.4 ± 0.08 m to 0.7 ± 0.05 m in the Ka band from ASUMA to EAIIST areas, and from 16.2 ± 1.0 m to 9.5 ± 1.4 m in the Ku band. In S band, δ_{p} is larger than the size of the snowpack (100 m) due to the very low ice absorption and the absence of volume scattering. The δ_{p} only accounts for absorption and scattering by snow grains and overestimates the penetration depth of the radar signal. δ_{p} values are consistent with previous studies that estimated values from 7 m within the continent to 15 m at a lower altitude in the Ku band (Davis and Moore, 1993, Legrésy and Rémy, 1998).

To understand the cause of the d_{EGC} variations between ASUMA and EAIIST areas, Table 3 shows the average values of the extinction coefficients κ_e for EAIIST and ASUMA traverses, and the partition between the scattering coefficient κ_s that is controlled by SSA and density values, and the absorption coefficient κ_a that depends on snow temperature and density (Zwally, 1989, Mätzler, 1998). κ_s is larger at all bands on EAIIST due to the coarser grains on the central Plateau (smaller SSA, see Table 1). Moreover, the impact of scattering on κ_e is higher than the impact of absorption in the Ka band (largest κ_s values, Table 3) because of the large contribution of the scattering to the extinction when the snow grain size is close to the radar wavelength. The opposite is to be noted for the absorption coefficient, κ_a increases from EAIIST to ASUMA areas because of higher temperatures closer to the coast. Besides,

Table 2: Depth of the echo gravity center (d_{EGC}) and the e-folding depth (δ_{p}) for all site and in the Ka, Ku and S bands. The '^{A}' or '^{E}' superscripts refer to the ASUMA and EAIIST traverses.

site	d_{EGC} Ka [m]	d_{EGC} Ku [m]	d_{EGC} S [m]	δ_{p} Ka [m]	δ_{p} Ku [m]	δ_{p} S [m]
stop5^A	0.9	3.7	-	1.5	14.9	-
charcot^A	0.4	4.7	-	1.4	17.4	-
stop0^A	1.0	2.5	4.6	1.3	16.9	>100
stop2^A	1.3	2.7	3.0	1.4	15.9	>100
stop3^A	1.0	3.7	-	1.3	15.8	-
ago5^E	0.3	3.2	5.8	0.6	8.5	>100
paleo^E	0.4	3.2	-	0.7	10.5	-

the impact of absorption is larger on κ_e than the impact of scattering in the S band (largest κ_a values, Table 3).

As a result, in the Ka band, κ_e is higher for the EAIIST area due to larger snow grain sizes, leading to lower wave penetration depth compared to that of the ASUMA area. In the S band, κ_e is larger for the ASUMA area due to higher temperatures, leading to smaller wave penetration depths compared to the EAIIST area. The sensitivity of the penetration depth in the Ku band is more complex and intermediate because of the balanced contribution of scattering and absorption. It is more sensitive to the snow temperature on ASUMA because the absorption dominates the extinction, and it is more sensitive to SSA on EAIIST where scattering is very strong.

5. Discussion

5.1. Spatial variations of snowpack properties

In this study, we observed a clear increase of waveform amplitudes from the coast to the interior of the continent, with a significant difference of 4 dB, 3 dB and 5 dB of σ^0 at Ka, Ku and S bands, respectively. This is in agreement with former observations of Remy et al. (2012) and Legresy et al. (2005), but

Table 3: Average values of coefficients κ_s, κ_a and κ_e (in m^{-1}) for EAIIST and ASUMA sites in the Ka, Ku and S bands. Average values of snow density, SSA, snow temperature are detailed in Table 1.

Traverse	Ka band			Ku band			S band		
	κ_s	κ_a	κ_e	κ_s	κ_a	κ_e	κ_s	κ_a	κ_e
ASUMA	0.5	0.3	0.8	$9.5\,10^{-3}$	$4.9\,10^{-2}$	$5.8\,10^{-2}$	$2.8\,10^{-5}$	$2.8\,10^{-3}$	$2.8\,10^{-3}$
EAIIST	3.4	0.2	3.6	$5.4\,10^{-2}$	$3.4\,10^{-2}$	$8.8\,10^{-2}$	$2.0\,10^{-4}$	$1.8\,10^{-3}$	$2.0\,10^{-3}$

the cause remains to be elucidated. Based on our sensitivity analysis, we have identified the variables that may play a direct role in this pattern, namely the roughness, density and SSA. However other indirect roles can be involved as well (such as slopes and temperatures). As pointed out by Adodo et al. (2018), the temperature has a weak direct effect on the waveform but can play a significant indirect role because it controls the typical SSA and density in a location through snowfall, metamorphism, and post-deposit processes that themselves are very temperature-sensitive (Picard et al., 2012). This results in potential multiple tangled causes to explain the 4 dB gradient depending on the local meteorological conditions. Here we discuss how the meteorological conditions affect the waveforms.

Remy et al. (2012) explained the lower σ^0 close to the coastal areas by the presence of persistent katabatic winds, high accumulation rate, and the significant slopes as follows:

- The strong winds near the coast tend to carve rough surfaces and increase the snow density. Legrésy and Rémy (1997) linked the decrease of roughness features to the increasing waveform amplitude observed from the coast to the interior of the continent, which is consistent with our results. This effect seems to dominate over the effect of the near-surface snow density. Indeed, the density decreases southward – as shown by our measurements and based on the wind gradient – and should results in smaller waveform amplitudes due to the decreased surface scattering (Section 4.5). However, the opposite is observed. The dominant effect of surface roughness can be explained by the fact that a dense snow surface amplifies the effects of roughness on the measured echo by increasing the effective dielectric discontinuity.

- the degree of layering in the snowpack depends on the snow accumulation rate that is still poorly known in the Antarctic ice sheet (Frezzotti et al., 2005). As mentioned by Rémy and Parouty (2009), this rate is a function of snow precipitation and compaction that varies with erosion, drift, deposition by the wind or sublimation and all these processes are not very well known. The waveform amplitude increases when the snowpack is highly stratified because it leads to more intense and numerous reflections at internal interfaces. Legrésy and Rémy (1997) reported that the lower accumulation rate in the central Plateau contributed to high waveform amplitudes with large internal reflections. This accumulation rate gradient is consistent with the higher variability in our measured density profiles (Fig. 3) in the central Plateau, and with our result showing that interface contributions on the total echo are larger in the interior of the continent. Besides, we have shown that this sensitivity to the internal reflections is particularly high in the S band because the signal penetrates deeply (Fig. 7). Thus, in the Ku and S bands, the larger σ^0 over the central Plateau may be due to the stronger internal reflections caused by the higher stratification and smoother interfaces.

- The surface slope shifts the closest point from the nadir and greatly decreases the backscattered energy when the slopes are larger than the antenna aperture (Legresy et al., 2005). The slope generally increases from the central Plateau to the coastal areas, and this contributes to the low waveform amplitudes near the coast. In this study, the two steepest sites are charcot^A and stop3^A in the ASUMA area, and indeed have the lowest observed and simulated waveform amplitudes (Fig 6). As a consequence, the topography also strongly contributes to the σ^0 variations. In particular, here we have shown that the waveform shape may be impacted when the surface slope is above 0.2°, as it probably highly contributes to large elevation bias retrieved for stop3^A in Section 4.4. Note that the slope effect can be frequency-dependent due to the usually larger antenna aperture at lower frequencies (Remy et al., 1996, Rémy and Parouty, 2009).

Several studies also found that an increase of the snow grain size and snow temperature increases the scattering and dielectric losses, and so the extinction strength (Rémy and Parouty, 2009, Lacroix et al., 2008a, Remy et al., 2012, Arthern et al., 2001, Michel et al., 2014, Adodo et al., 2018). Davis and Moore (1993) showed that the wave penetration depth on the central Plateau is mainly dominated by the snow grain scattering. However, contrary to our results they found larger penetration depths on the central Plateau than near the coast and explained that it was due to larger snow grain sizes close to the coast. Here we have shown that over the central Plateau the grains are larger, which was also found out by (Brucker et al., 2010) using microwave data. This induces a smaller wave penetration depth in the Ka and Ku bands than it is close to the coast. This latter result was fully supported by both in-situ measurements and simulations.

5.2. Toward inversions with active and passive data

The main challenge in the altimetry ice sheet is to correct surface elevation retrieved from altimeter observations when the snow parameters are unknown at the global scale. Following our sensitivity analysis, for a relatively flat surface the main parameters to optimize for routine measurements would be the surface roughness, the density, and the SSA. Note that, as recommended by Lacroix et al. (2008a), in the area with large slopes the waveform parameters must first be corrected for the topographic effect, before fitting the model. Here we propose two synthetic snowpacks that would be good first approximations of the real snowpacks for the central Plateau and areas close to the coast for inversion processes. Using our large latitudinal range of measurement, we simply averaged the snow parameters (5 sites for ASUMA and 2 sites for EAIIST) to represent the two synthetic snowpacks. Of course, these two snowpacks are not realistic for the entire area but to the best of our knowledge, this is the most representative that we can get due to the lack of information, and at least it would minimize the search space of each parameter in the optimization process. For areas in the central Plateau, the initial value of MSS can be prescribed to 0.01, the density profile can be represented with a profile extrapolated from 335 $\mathrm{kg\,m^{-3}}$ at the surface to 422 $\mathrm{kg\,m^{-3}}$ at 8 m, and the SSA profile with a profile extrapolated from 15 $\mathrm{m^{-2}\,kg^{-1}}$ to 6 $\mathrm{m^{-2}\,kg^{-1}}$ from the surface to 8 m depth. For areas close to the coast, the MSS can be set to 0.03, the density profile can be represented with a profile extrapolated from 412 $\mathrm{kg\,m^{-3}}$ at the surface to 487 $\mathrm{kg\,m^{-3}}$ at 8 m, and the SSA with a profile extrapolated from 28 $\mathrm{m^{-2}\,kg^{-1}}$ to 9 $\mathrm{m^{-2}\,kg^{-1}}$. Layer thicknesses are 10 cm.

The retrieval of snow parameters by the inversion of altimeter models as complex as SMRT is difficult since some waveform changes are the combination of several effects that can hardly be distinguished without ancillary in-situ information: snow grain size and density variations can have the same impact on the waveform shape, for instance leading to a larger LeW, while the surface roughness would have an opposite effect on the LeW. This aspect was observed in Section 4.5 as well as in previous studies (Rémy and Parouty, 2009). To address this issue, a perspective is to combine both passive and active observations in the inversion process to better constrain snow parameters (Flach et al., 2005). Indeed, in the Antarctic ice sheet, while the active observations are mainly sensitives to the surface roughness, snow density, and snow grain size, the passive observations are mainly sensitives to the snow grain size (for dry snow). Several studies developed methods to invert electromagnetic models in the passive mode to retrieve the effective snow grain size (Picard et al., 2014, Brucker et al., 2010). Following the method developed in Brucker et al. (2010), the optical radius of snow grains could be fitted with passive microwave observations at 19 GHz and 37 GHz using SMRT. The surface roughness and density could then be fitted using altimetry observations as proposed in Lacroix et al. (2008a). While Lacroix et al. (2008a) performed the inversion using 3 waveform parameters, we advise using the whole waveform shape (Partington et al., 1989, **?**). Although a full validation of this approach is out of the scope of this paper and left for future work, this approach is an interesting perspective to get waveform shapes closer to the altimeter observations when no in situ snow properties are known.

5.3. Limitations of assumptions and perspectives

SMRT can now be used as a sophisticated altimeter model adapted for multiple-layers snowpack and offering the choice between several electromagnetic and surface scattering models. However, several assumptions had to be made for SMRT simulations and are summarized in Section 2.4. Here we discuss the limitation of the assumptions and perspectives for future developments in SMRT:

- The new altimeter extension of SMRT developed in this study is limited to single scattering (first-order solution of the radiative transfer equation using the iterative method), and multiple scattering between the snowpack and the substrate (or between interfaces) can not be accounted for with this model. At low frequencies (S band), the consideration of first-order scattering only is sufficient since scattering is weak compared to absorption, as shown in Section 4.6. However, the effect of multiple scattering at high frequency (Ka band) may be significant. Implementing the full bi-directional advanced IEM (AIEM) is a perspective to account for multiple scattering.

- In SMRT simulations, ice grains are spherical and the optical radius of grains is scaled by a constant factor of 2.3. In reality, ice grains are not spherical and this scaling factor may change spatially according to snow properties. An alternative is to invert SMRT with passive microwave observations as in Brucker et al. (2010) to get an effective optical radius per site closer of the real snow microstructure.

- The validity domain of the GO approximation requires that the centimeter-roughness scale (above 10 cm) is large enough compared to the incident wavelength. This assumption is reasonable for the Ku and Ka bands, but is questionable for the S band (9.4 cm wavelength). Given that the roughness rms heights measured from the in-situ DEM were larger than 10 cm for our studied sites, the S band is in the validity range of GO but is outside IEM. Besides, previous studies also suggest that sastrugi - with a 10 cm to 1 mm height - are the major contributors to surface scattering in the Ka-S bands in the Antarctic ice sheet (Inoue, 1989, Lacroix et al., 2007).

- Due to the vertical precision of the photogrammetric camera setup and the horizontal spacing of measurements (9 cm), we had no information about the roughness at scales below 9 cm. The measurement technique can overlook the sub-centimeter roughness scales that may impact the radar waveform in the Ka-Ku bands. Nevertheless, the visual inspection of the surface suggests that the surface is usually smooth at the smaller scales and that most of the slopes are due to the large-scale roughness captured by the camera. This is not sufficient to conclude that the electromagnetic effect is negligible. For a more precise assessment, measurements would be needed. However, these small surface roughness features are difficult to measure, as mentioned by Rémy and Parouty (2009). This question remains open to further investigation.

- In the absence of interface roughness information at a centimeter scale, we also assumed that the buried interfaces have the same roughness as at the surface, despite some possible smoothing effects due to compaction and snow metamorphism. To verify that this assumption is reasonable, we evaluated the model sensitivity to varied MSS values for internal interfaces when the surface MSS value is fixed (not shown). Compared to simulations with the same MSS value for interfaces and surface, we estimated that a decrease of 20% of the interface MSS values - when the surface MSS is fixed - induces an increase of the interface contributions to the total echo by 3% and 5% in the Ku and S bands, respectively. The change in the Ka band is negligible. For all bands and sensors, the shape of the simulated waveforms is not impacted. Therefore, the assumption is acceptable.

6. Summary and conclusion

This study extended an existing snow radiative transfer model (SMRT) for altimetry applications over snow-covered surfaces. Driven by in-situ measurements of density and SSA profiles, annual mean temperature, and a surface roughness parameter (Mean Square Slope) acquired on the Antarctic ice sheet, waveforms are simulated in the Ka, Ku, and S bands. The results show a good agreement with satellite observations, with correlation coefficients higher than 0.6 for the σ^0 retrieved from normalized simulated waveforms with the ICE-1 retracker. Moreover, SMRT reproduces the observed waveform shapes well, and can simulate the returned power from the surface, the internal interfaces, and the snow grains separately which helps to investigate the radar signal behavior according to the studied frequency and site characteristics. Our main results show that for the waveform amplitude variations (i.e. σ^0):

- The surface echo is the main contribution for all sites and sensors. Because the surface is smoother, the waveform amplitude is higher in the central Plateau than near the coast for all sensor configurations.

- The volume echo (i.e. caused by snow grain scattering) represents up to 40% of the total echo in the Ka band and decreases at lower frequencies to become negligible in the S band. In the Ka band, the amplitude of the volume echo is higher in the central Plateau due to the larger snow grains.

- The interface contribution is negligible in the Ka band and increases at lower frequencies (about 25-50% of the total echo in the S band). In the S Band, the amplitude of the interface echo is higher in the central Plateau due to a more stratified snowpack.

In the Ka band, the elevation biases retrieved with the ICE1 retracking algorithm appear homogeneous on the investigated area and equal to 10.2 ± 2.2 cm. Compared to closer to the coast, in the interior of the continent, the snowpack is less dense and has larger snow grains, which increases the elevation bias, but at the same time, the surface is smoother, which partially counterbalances this effect. In the Ku band, the impact of the larger density and SSA is stronger since the wave penetrates deeper, so that the elevation bias is twice larger in the central Plateau compared to that close to the coast (10.6±3.6 cm close to the coast, and 21.2±4.0 cm in the central Plateau).

The differences between the observed and simulated waveforms may be due to the use of local in-situ measurements to drive the model while satellite observations represent a larger scale. The sensitivity analysis shows that the roughness and density are the main drivers of the waveform, in particular at low frequency. For instance, an error of ± 20% in the measured values leads to ± 30% variations in the waveform amplitude in the S band at stop2^A. By readjusting the Mean Square Slope values with satellite observations instead of using the measured values, the simulated σ^0 is significantly improved in the Ku and S bands, and we found that a constant MSS value of 0.03 for areas close to the coast, and 0.01 in the interior of the continent are good first approximations when no roughness measurements are available.

This altimeter extension of SMRT offers new opportunities to better interpret the signal according to the snowpack properties, in particular for analyzing the complex relationship between the geophysical parameters and the wave penetration depth that is a major cause of surface elevation uncertainties in the polar ice sheet mass balance. The first analysis shows that in the Ka and Ku bands, the penetration depth of the wave is lower in the central Plateau than near the coast because of the bigger snow grains that result in large scattering, while in the S band, the penetration depth is larger in the central Plateau than near the coast due to lower snow temperature.

The retrieval of geophysical parameters from the observed waveforms remains a challenging task because the relationships between the snow parameters and the waveform shape are complex and inter-dependent. Using the passive and active mode of SMRT is an interesting perspective to retrieve snowpack parameters when no in-situ data are available. Further work is needed to evaluate the retracking algorithms in combination with SMRT simulations. Moreover, because SMRT can represent a large variety of cold environments, altimeter simulations can now be run for sea-ice and lake-ice, and therefore contribute to developing algorithms for snow depth retrievals over sea ice using a multi-frequency combination for instance. Another avenue is to extend SMRT for the high-resolution SAR altimetry mode, which would make it suitable to the simulation of Sentinel-3A, CryoSat-2, and Sentinel-6 signals.

Author contributions

FL and GP contributed to the conception and design of the work. All authors contributed to the analysis, and interpretation of data. GP developed the altimetry extension in SMRT, FL wrote the manuscript. VF, BJ, JS, LA, EL, GP and FL acquired measurements in Antarctica.

Appendix

δ: Dirac distribution

δ_{p}: e-folding depth

Δt: travel time between each altimeter gate

κ_e: extinction coefficient

κ_a: absorption coefficient

κ_s: scattering coefficient

λ: radar wavelength

Ω: solid angle from the sensor to the elementary area

ψ: incident zenith angle

ϕ: incident azimuth angle

ρ: horizontal distance between the z axis and the elementary area reached at time t

σ^0: total backscattering coefficient

σ^0_{int}: backscattering coefficient of the interfaces

σ^0_s: backscattering coefficient of the surface

σ_{surf} : root mean square heights (rms) of the surface roughness

$\sigma^0_{\mathrm{int}}(\theta, z_n)$: backscattering coefficient of the interface at depth z_n

θ: angle from the antenna boresight axis to the line from the sensor to the elementary area

θ_0: incident zenith angle

θ_s: local slope

$A_{i,\nu}$: waveform amplitude of site i at the frequency ν estimated with the ICE-A retracker algorithm

c: speed of the wave in the medium

c_0: speed of the wave in air

d_{EGC}: echo gravity center depth

$E_0(\theta_0, z, t)$: the incident flux

g: altimeter gate index

$\mathrm{G}(\theta)$: the antenna pattern function

g_{EGC}: gate position of the echo gravity center of the total backscattering intensity

H : altimeter elevation

$I'(\mathbf{r})$: specific intensity of the wave or radiance

$I(\mathbf{r})$: reduced specific intensity of the wave

I_{int}: reduced specific intensities coming from the interface reflection

I_{vol}: reduced specific intensities coming from volume scattering

$I^{0^{\mathrm{th}}}$: 0^{th}-order intensity at depth z

I_{TOT}: total backscattering intensity (sum of volume and interface backscattering intensities)

$I_{\mathrm{vol}}^{1^{\mathrm{st}}}(z = 0, t)$: 1^{st}-order solution of the radiative transfer equation only including the direct backscattered wave emerging at the surface from volume scattering

$I_{\mathrm{n,\ vol}}^{1^{\mathrm{st}}}(z = 0, t)$: volume backscattered intensity emerging at the surface and coming from the sublayer n

$I_{\mathrm{n,\ int}}^{1^{\mathrm{st}}}(z = 0, \theta, t)$: backscattered intensity from the internal interfaces emerging at the surface and coming from the sublayer n

l: snow layer index

LEP_{surf}: leading-edge position defined with a 50% of the waveform amplitude of the surface echo

LEP_{TOT}: leading-edge position defined with a 50% of the waveform amplitude of the total echo

LeW: Leading-edge width of the radar waveform

$n(\mathbf{r})$: refractive index

P: phase matrix

$P(0,0,\pi,z)$: scattering function from snow grains in the backward direction at nadir incidence

$P_{\mathrm{FIR}}(t)$: flat impulse response

P_{FS}: flat impulse response of the surface echo

P_{int}: flat impulse response of the echoes from the internal interfaces

P_r: total returned power

P_t: transmitted signal power

P_{vol}: flat impulse response of the echoes from the scattering by snow grains

pdf: point distribution function

r: distance between the sensor and the elementary area

$\mathbf{r}_l^+$: position just above the layer interface at a distance r_l

$\mathbf{r}_l^-$: position just below the layer interface at a distance r_l

$R(\mathbf{r}_l,\theta)$: reflection coefficient at the position $\mathbf{r}_l$

s: the curvilinear abscissa along the trajectory

$T(\mathbf{r}_l,\theta)$: transmittance for the reduced specific intensity) at the position $\mathbf{r}_l$

$T(z_l)$: interface transmittance at the layer depth z_l

t': two-way time between the altimeter and the wave hit position in the snowpack

t_s: two-way time between the altimeter and the wave hit position on the surface

z_l: depth of the layer l

Acknowledgments

This study was supported by the EAIIST project (ANR-16-CE01-0011), the Institut Polaire Français Paul-Emile Victor (IPEV), the National Antarctic Research Program (PNRA), the French Research National Agency (Project ANR program 1-JS56-005-01 MONISNOW, ANR-14-CE01-0001 ASUMA, ANR-07-VULN-013 VANISH). The BNP-Paribas foundation is also acknowledged for providing EAIIST funding through its Climate Initiative program. We acknowledge the European Space Agency (ESA) for the financial support allowing the initial development of SMRT (ESTEC:4000112698/14/NL/LvH) and the altimeter extension (Polar Monitoring Mission project, ESTEC:4000126504/19/NL/NA). The authors would like to warmly thank all the participants of the ASUMA and EAIIST traverses for their tremendous field contributions allowing the collection of the crucial in-situ measurements used in this study.

References

Adams, R.J., Brown, G.S., 1998. A model for altimeter returns from penetrable geophysical media. IEEE Transactions on Geoscience and Remote Sensing 36, 1784–1793. doi:`10.1109/36.718645`.

Adodo, F.I., Remy, F., Picard, G., 2018. Seasonal variations of the backscattering coefficient measured by radar altimeters over the Antarctic Ice Sheet. The Cryosphere 12, 1767–1778. doi:`10.5194/tc-12-1767-2018`.

Agisoft, 2019. Agisoft Metashape User Manual. Professionnal Edition, Version 1.5. Technical Report. URL: `https://www.agisoft.com/pdf/metashape-pro_1_5_en.pdf`. last access: Septembre 2020.

Arnaud, L., Picard, G., Champollion, N., Domine, F., Gallet, J., Lefebvre, E., Fily, M., Barnola, J., 2011. Measurement of vertical profiles of snow specific surface area with a 1 cm resolution using infrared reflectance: instrument description and validation. Journal of Glaciology 57, 17–29. doi:`10.3189/002214311795306664`.

Arthern, R.J., Wingham, D.J., Ridout, A.L., 2001. Controls on ers altimeter measurements over ice sheets: Footprint-scale topography, backscatter fluctuations, and the dependence of microwave penetration depth on satellite orientation. Journal of Geophysical Research: Atmospheres 106, 33471–33484. doi:`10.1029/2001JD000498`.

Belem, T., Homand-Etienne, F., Souley, M., 2000. Quantitative parameters for rock joint surface roughness. Rock Mechanics and Rock Engineering 33, 217–242. doi:`10.1007/s006030070001`.

Bindschadler, R., Zwally, H., 1986. Surface Topography of the Greenland Ice Sheet by Satellite Radar Altimetry (Abstract). Annals of Glaciology 8, 196–196. doi:`10.3189/s0260305500001452`.

Brenner, A.C., Bindschadler, R.A., Thomas, R.H., Zwally, H.J., 1983. Slope-induced errors in radar altimetry over continental ice sheets. Journal of Geophysical Research 88, 1617–1623. doi:`10.1029/JC088iC03p01617`.

Brown, G.S., 1977. The Average Impulse Response of a Rough Surface and Its Applications. IEEE Journal of Oceanic Engineering 2, 67–74. doi:`10.1109/JOE.1977.1145328`.

Brucker, L., Picard, G., Fily, M., 2010. Snow grain-size profiles deduced from microwave snow emissivities in antarctica. Journal of Glaciology 56, 514–526. doi:`10.3189/002214310792447806`.

Davis, C.H., Moore, R.K., 1993. A combined surface- and volume-scattering model for ice-sheet radar altimetry. Journal of Glaciology 39, 675–686. doi:`10.3189/s0022143000016579`.

Femenias, P., Remy, F., Raizonville, R., Minster, J.F., 1993. Analysis of satellite-altimeter height measurements above continental ice sheets. Journal of Glaciology 39, 591–600. doi:`10.3189/S0022143000016488`.

Flach, J.D., Partington, K.C., Ruiz, C., Jeansou, E., Drinkwater, M.R., 2005. Inversion of the surface properties of ice sheets from satellite microwave data. IEEE Transactions on Geoscience and Remote Sensing 43, 743–752. doi:`10.1109/TGRS.2005.844287`.

Frezzotti, M., Pourchet, M., Flora, O., Gandolfi, S., Gay, M., Urbini, S., Vincent, C., Becagli, S., Gragnani, R., Proposito, M., et al., 2005. Spatial and temporal variability of snow accumulation in east antarctica from traverse data. Journal of Glaciology 51, 113–124. doi:`10.3189/172756505781829502`.

Fung, A.K., Li, Z., Chen, K., 1992. Backscattering from a randomly rough dielectric surface. IEEE Transactions on Geoscience and Remote Sensing 30, 356–369.

Gallet, J.C., Domine, F., Arnaud, L., Picard, G., Savarino, J., 2011. Vertical profile of the specific surface area and density of the snow at Dome C and on a transect to Dumont D'Urville, Antarctica - Albedo calculations and comparison to remote sensing products. The Cryosphere 5, 631–649. doi:`10.5194/tc-5-631-2011`.

Gay, M., Ferro-Famil, L., 2016. Penetration depth of Synthetic Aperture Radar signals in ice and snow: an analytical approach, in: Workshop Remote Sensing and Modeling of Surface Properties, Grenoble, France. URL: `https://hal.archives-ouvertes.fr/hal-01535482`.

Gharechelou, S., Tateishi, R., Johnson, B.A., 2018. A simple method for the parameterization of surface roughness from microwave remote sensing. Remote Sensing 10, 1711. doi:`10.3390/rs10111711`.

Guerreiro, K., Fleury, S., Zakharova, E., Kouraev, A., Rémy, F., Maisongrande, P., 2017. Comparison of cryosat-2 and envisat radar freeboard over arctic sea ice: toward an improved envisat freeboard retrieval. The Cryosphere 11, 2059–2073. doi:`10.5194/tc-11-2059-2017`.

Guerreiro, K., Fleury, S., Zakharova, E., Rémy, F., Kouraev, A., 2016. Potential for estimation of snow depth on Arctic sea ice from CryoSat-2 and SARAL/AltiKa missions. Remote Sensing of Environment 186, 339–349. doi:`10.1016/j.rse.2016.07.013`.

Helm, V., Humbert, A., Miller, H., 2014. Elevation and elevation change of Greenland and Antarctica derived from CryoSat-2. The Cryosphere 8, 1539–1559. doi:`10.5194/tc-8-1539-2014`.

Hersbach, H., Bell, B., Berrisford, P., Hirahara, S., Horányi, A., Muñoz-Sabater, J., Nicolas, J., Peubey, C., Radu, R., Schepers, D., Simmons, A., Soci, C., Abdalla, S., Abellan, X., Balsamo, G., Bechtold, P., Biavati, G., Bidlot, J., Bonavita, M., De Chiara, G., Dahlgren, P., Dee, D., Diamantakis, M., Dragani, R., Flemming, J., Forbes, R., Fuentes, M., Geer, A., Haimberger, L., Healy, S., Hogan, R.J., Hólm, E., Janisková, M., Keeley, S., Laloyaux, P., Lopez, P., Lupu, C., Radnoti, G., de Rosnay, P., Rozum, I., Vamborg, F., Villaume, S., Thépaut, J.N., 2020. The era5 global reanalysis. Quarterly Journal of the Royal Meteorological Society 146, 1999–2049. doi:`10.1002/qj.3803`.

Howat, I.M., Porter, C., Smith, B.E., Noh, M.J., Morin, P., 2019. The reference elevation model of antarctica. The Cryosphere 13, 665–674. doi:`10.5194/tc-13-665-2019`.

Inoue, J., 1989. Surface drag over the snow surface of the antarctic plateau: 1. factors controlling surface drag over the katabatic wind region. Journal of Geophysical Research: Atmospheres 94, 2207–2217. URL: `https://agupubs.onlinelibrary.wiley.com/doi/abs/10.1029/JD094iD02p02207`, doi:`https://doi.org/10.1029/JD094iD02p02207`, `arXiv:https://agupubs.onlinelibrary.wiley.com/doi/pdf/10.1029/JD094iD02p02207`.

Irvine-Fynn, T.D., Sanz-Ablanedo, E., Rutter, N., Smith, M.W., Chandler, J.H., 2014. Measuring glacier surface roughness using plot-scale, close-range digital photogrammetry. Journal of Glaciology 60, 957–969. doi:`10.3189/2014JoG14J032`.

Kerr, T., Owens, I., Rack, W., Gardner, R., 2009. Using ground-based laser scanning to monitor surface change on the Rolleston glacier, New Zealand. Journal of Hydrology (New Zealand) 48, 59–72. Retrieved October 2, 2020, from http://www.jstor.org/stable/43944978.

Kurtz, N.T., Galin, N., Studinger, M., 2014. An improved CryoSat-2 sea ice freeboard retrieval algorithm through the use of waveform fitting. The Cryosphere 8, 1217–1237. doi:`10.5194/tc-8-1217-2014`.

Lacroix, P., Dechambre, M., Legrésy, B., Blarel, F., Rémy, F., 2008a. On the use of the dual-frequency ENVISAT altimeter to determine snowpack properties of the Antarctic ice sheet. Remote Sensing of Environment 112, 1712–1729. doi:`10.1016/j.rse.2007.08.022`.

Lacroix, P., Legrésy, B., Coleman, R., Dechambre, M., Rémy, F., 2007. Dual-frequency altimeter signal from Envisat on the Amery ice-shelf. Remote Sensing of Environment 109, 285–294. doi:`10.1016/j.rse.2007.01.007`.

Lacroix, P., Sy, B.L., Langley, K., Hamran, S.E., Kohler, J., Roques, S., Ré My, F., Dechambre, M., 2008b. Instruments and methodsin situ measurements of snow surface roughness using a laser profiler. Journal of Glaciology 54, 753–762. doi:`10.3189/002214308786570863`.

Legresy, B., Papa, F., Remy, F., Vinay, G., Van Den Bosch, M., Zanife, O.Z., 2005. ENVISAT radar altimeter measurements over continental surfaces and ice caps using the ICE-2 retracking algorithm. Remote Sensing of Environment 95, 150–163. doi:`10.1016/j.rse.2004.11.018`.

Legrésy, B., Rémy, F., 1997. Altimetric observations of surface characteristics of the antarctic ice sheet. Journal of Glaciology 43, 265–275. doi:`10.3189/S002214300000321X`.

Legrésy, B., Rémy, F., 1998. Using the temporal variability of satellite radar altimetric observations to map surface properties of the antarctic ice sheet. Journal of Glaciology 44, 197–206. doi:`10.3189/S0022143000002537`.

Li, S., Zhao, D., Zhou, L., Liu, B., 2013. Dependence of mean square slope on wave state and its application in altimeter wind speed retrieval. International Journal of Remote Sensing 34, 264–275. doi:`10.1080/01431161.2012.713144`.

Libois, Q., Picard, G., Arnaud, L., Dumont, M., Lafaysse, M., Morin, S., Lefebvre, E., 2015. Summertime evolution of snow specific surface area close to the surface on the Antarctic Plateau. The Cryosphere 9, 2383–2398. doi:`10.5194/tc-9-2383-2015`.

MacArthur, J., 1978. SEASAT: A Radar Altimeter Design Description. Johns Hopkins University Applied Physics Laboratory.

Marks, A.A., King, M.D., 2014. The effect of snow/sea ice type on the response of albedo and light penetration depth (e-folding depth) to increasing black carbon. The Cryosphere 8, 1625–1638. URL: `https://tc.copernicus.org/articles/8/1625/2014/`, doi:`10.5194/tc-8-1625-2014`.

Matsuoka, T., Fujita, S., Mae, S., 1996. Effect of temperature on dielectric properties of ice in the range 5–39 ghz. Journal of Applied Physics 80, 5884–5890. doi:`10.1063/1.363582`.

Mätzler, C., 1998. Improved Born approximation for scattering of radiation in a granular medium. Journal of Applied Physics 83, 6111–6117. doi:`10.1063/1.367496`.

Mätzler, C., Wegmuller, U., 1987. Dielectric properties of freshwater ice at microwave frequencies. Journal of Physics D: Applied Physics 20, 1623–1630. doi:`10.1088/0022-3727/20/12/013`.

Michel, A., Flament, T., Rémy, F., 2014. Study of the penetration bias of ENVISAT altimeter observations over Antarctica in comparison to ICESat observations. Remote Sensing 6, 9412–9434. doi:`10.3390/rs6109412`.

Newkirk, M.H., Brown, G.S., 1992. Issues related to waveform computations for radar altimeter applications. IEEE Transactions on antennas and propagation 40, 1478–1488. doi:`10.1109/8.204738`.

Nield, J.M., Chiverrell, R.C., Darby, S.E., Leyland, J., Vircavs, L.H., Jacobs, B., 2013. Complex spatial feedbacks of tephra redistribution, ice melt and surface roughness modulate ablation on tephra covered glaciers. Earth Surface Processes and Landforms 38, 95–102. doi:`10.1002/esp.3352`.

Partington, K., Ridley, J., Rapley, C., Zwally, H., 1989. Observations of the surface properties of the ice sheets by satellite radar altimetry. Journal of Glaciology 35, 267–275. doi:`10.3189/S0022143000004603`.

Picard, G., Arnaud, L., Domine, F., Fily, M., 2009. Determining snow specific surface area from near-infrared reflectance measurements: Numerical study of the influence of grain shape. Cold Regions Science and Technology 56, 10–17. doi:`10.1016/J.COLDREGIONS.2008.10.001`.

Picard, G., Domine, F., Krinner, Arnaud, L., Lefebvre, 2012. Inhibition of the positive snow-albedo feedback by precipitation in interior antarctica. Nature Climate Change 2, 795–798. doi:`10.1038/nclimate1590`.

Picard, G., Royer, A., Arnaud, L., Fily, M., 2014. Influence of meter-scale wind-formed features on the variability of the microwave brightness temperature around Dome C in Antarctica. The Cryosphere 8, 1105–1119. doi:`10.5194/tc-8-1105-2014`.

Picard, G., Sandells, M., Löwe, H., 2018. Smrt: an active–passive microwave radiative transfer model for snow with multiple microstructure and scattering formulations (v1.0). Geoscientific Model Development 11, 2763–2788. doi:`10.5194/gmd-11-2763-2018`.

Picard, G., R.A.A.L., Fily, M., 2014. Influence of meter-scale wind-formed features on the variability of the microwave brightness temperature around dome c in antarctica. The Cryosphere 8, 1105–1119. doi:`10.5194/tc-8-1105-2014`.

Remy, F., Flament, T., Blarel, F., Benveniste, J., 2012. Radar altimetry measurements over antarctic ice sheet: A focus on antenna polarization and change in backscatter problems. Advances in Space Research 50, 998–1006. doi:`10.1016/j.asr.2012.04.003`.

Remy, F., Legresy, B., Bleuzen, S., Vincent, P., Minster, J., 1996. Dual-frequency topex altimeter observations of greenland. Journal of Electromagnetic Waves and Applications 10, 1507–1525. URL: `https:`

//doi.org/10.1163/156939396X00892, doi:10.1163/156939396X00892, arXiv:https://doi.org/10.1163/156939396X00892.

Remy, F., Minster, J.F., 1991. A comparison between active and passive microwave measurements of the antarctic ice sheet and their association with the surface katabatic winds. Journal of Glaciology 37, 3–10. doi:10.3189/S0022143000042738.

Rémy, F., Parouty, S., 2009. Antarctic ice sheet and radar altimetry: A Review. Remote Sensing 1, 1212–1239. doi:10.3390/rs1041212.

Rosmorduc, V., Benveniste, J., Lauret, O., Maheu, C., Milagro, M., Picot, N., 2011. Radar altimetry tutorial. http://www.altimetry.info/radar-altimetry-tutorial/ Last access: October 2020.

Roy, A., Picard, G., Royer, A., Montpetit, B., Dupont, F., Langlois, A., Derksen, C., Champollion, N., 2013. Brightness temperature simulations of the canadian seasonal snowpack driven by measurements of the snow specific surface area. Geoscience and Remote Sensing, IEEE Transactions on 51, 4692–4704. doi:10.1109/TGRS.2012.2235842.

Schwegmann, S., Rinne, E., Ricker, R., Hendricks, S., Helm, V., 2016. About the consistency between envisat and cryosat-2 radar freeboard retrieval over antarctic sea ice. The Cryosphere 10, 1415–1425. doi:10.5194/tc-10-1415-2016.

Smith, M.W., Quincey, D.J., Dixon, T., Bingham, R.G., Carrivick, J.L., Irvine-Fynn, T.D.L., Rippin, D.M., 2016. Aerodynamic roughness of glacial ice surfaces derived from high-resolution topographic data. Journal of geophysical research: Earth Surface 121, 748–766. doi:10.1002/2015JF003759.Received.

Smith, M.W., Vericat, D., 2015. From experimental plots to experimental landscapes: topography, erosion and deposition in sub-humid badlands from structure-from-motion photogrammetry. Earth Surface Processes and Landforms 40, 1656–1671. doi:10.1002/esp.3747.

Studinger, M., Medley, B.C., Brunt, K.M., Casey, K.A., Kurtz, N.T., Manizade, S., Neumann, T.A., Overly, T.B., 2020. Temporal and spatial variability in surface roughness and accumulation rate around 88° s from repeat airborne geophysical surveys. The Cryosphere 14, 3287–3308. doi:`10.5194/tc-14-3287-2020`.

Tiuri, M.E., Sihvola, A.H., Nyfors, E.G., Hallikaiken, M.T., 1984. The Complex Dielectric Constant of Snow at Microwave Frequencies. IEEE Journal of Oceanic Engineering 9, 377–382. doi:`10.1109/JOE.1984.1145645`.

Tsang, L., Kong, Jin Au, ., Shin, R.T., 1985. Theory of microwave remote sensing. Wiley, New York. "A Wiley-Interscience publication.".

Tsang, L., Kong, J., Ding, K., Ao, O., 2001. Scattering of Electromagnetic Waves, Numerical Simulations. volume 2. John Wiley and Sons. doi:`10.1002/0471224308`.

Ulaby, F.T., Moore, R.K., Fung, A.K., 1986. Microwave Remote Sensing Active and Passive - Volume 3: From Theory to Applications. Artech House, Inc.

Van Der Veen, C.J., Ahn, Y., Csatho, B.M., Mosley-Thompson, E., Krabill, W.B., 2009. Surface roughness over the northern half of the Greenland Ice sheet from airborne laser altimetry. Journal of Geophysical Research: Earth Surface 114, 1–8. doi:`10.1029/2008JF001067`.

Van Der Veen, C.J., Krabill, W.B., Csatho, B.M., Bolzan, J.F., 1998. Surface roughness on the Greenland ice sheet from airborne laser altimetry. Geophysical Research Letters 25, 3887–3890. doi:`10.1029/1998GL900041`.

Vargel, C., Royer, A., St-Jean-Rondeau, O., Picard, G., Roy, A., Sasseville, V., Langlois, A., 2020. Arctic and subarctic snow microstructure analysis for microwave brightness temperature simulations. Remote Sensing of Environment 242, 111754. doi:`https://doi.org/10.1016/j.rse.2020.111754`.

Vaughan, D., Bamber, J., Giovinetto, M., Russell, J., Cooper, A., 1999. Reassessment of net surface mass balance in antarctica. Journal of Climate 12, 933–946.

Verron, J., Sengenes, P., Lambin, J., Noubel, J., Steunou, N., Guillot, A., Picot, N., Coutin-Faye, S., Sharma, R., Gairola, R.M., Murthy, D.V., Richman, J.G., Griffin, D., Pascual, A., Rémy, F., Gupta, P.K., 2015. The SARAL/AltiKa Altimetry Satellite Mission 38, 2–21. doi:`10.1080/01490419.2014.1000471`.

Wiesmann, A., Mätzler, C., 1999. Microwave emission model of layered snowpacks. Remote Sensing of Environment 70, 307 – 316. doi:`https://doi.org/10.1016/S0034-4257(99)00046-2`.

Wingham, D.J., Rapley, C.G., Griffiths, H., 1986. New Techniques in Satellite Altimeter Tracking Systems. Digest - International Geoscience and Remote Sensing Symposium (IGARSS) On Remote Sensing: Today's Solutions for Tomorrow's Information Needs, Volume 3 p 1339-1344.

Yang, J., Zhang, J., 2019. Validation of sentinel-3a/3b satellite altimetry wave heights with buoy and jason-3 data. Sensors 19, 2914. doi:`10.3390/s19132914`.

Yi, D., Bentley, C., 1994. Analysis of satellite radar-altimeter return wave forms over the east antarctic ice sheet. Annals of Glaciology 20, 137–142. doi:`10.3189/1994AoG20-1-137-142`.

Zelli, C., Aerospazio, A., 1999. Envisat ra-2 advanced radar altimeter: Instrument design and pre-launch performance assessment review. Acta Astronautica 44, 323 – 333. doi:`https://doi.org/10.1016/S0094-5765(99)00063-6`.

Zwally, H.J., 1989. Growth of Greenland Ice Sheet: Interpretation. volume 246. American Association for the Advancement of Science.